A Mesh Size Scaling Law with Reynolds Number for Large Eddy Simulation in Channel Flow

Jie Yao and C. J. Teo*

*Department of Mechanical Engineering, National University of Singapore,
9 Engineering Drive 1, Singapore 117575*

Abstract. In this paper, a scaling law relating the mesh size to the Reynolds number was proposed to ensure consistent results for large eddy simulation (LES) as the Reynolds number was varied. The grid size scaling law was developed by analyzing the lengthscale of the turbulent motion by using DNS data from the literature. The wall-resolving LES was then applied to a plane channel flow to validate the scaling law. The scaling law was tested at different Reynolds numbers ($Re_\tau = 395$, 590 and 1000), and showed good results compared to direct numerical simulation (DNS) in terms of mean flow and various turbulent statistics. The velocity spectra analysis shows the evidence of the Kolmogorov –5/3 inertial subrange and verifies that the current LES can resolve the bulk of the turbulent kinetic energy by satisfying the grid scaling law. Meanwhile, the near-wall turbulent flow structures can also be well captured. Reasonably accurate predictions can thus be obtained for flows at even higher Reynolds numbers with significantly lower computational costs compared to DNS by applying the mesh scaling law.

AMS subject classifications: 76F65
Key words: Large eddy simulation (LES), channel flow, turbulent flow, mesh size scaling law.

1 Introduction

Turbulence plays a dominant role in most engineering and natural flows. A turbulent flow is unsteady, chaotic and unpredictable, with the exact physical nature remaining mysterious. Thanks to the rapidly increasing computing power, Computational Fluid Dynamics (CFD) now offers a promising approach for calculating the relevant properties of turbulent flows. Direct numerical simulation (DNS) is one important method for the study of turbulent flows, which directly solves the Navier-Stokes equations (NS-equations) for all scales of motion. However, this approach is computationally too expensive, and is usually restricted to flows with relatively low Reynolds numbers. For

---

*Corresponding author.
Email: mpeteocj@nus.edu.sg (C. Teo)

numerical simulations with higher Reynolds numbers, turbulence is usually modelled. Reynolds averaged Navier–Stokes (RANS) models solve the Reynolds equations (mean-flow equations) to determine the mean velocity field by modelling the entire Reynolds stresses. RANS models have been used for various problems with turbulent flow involved, due to their ease of implementation and low computational cost. Large eddy simulation (LES) is another important approach, where the governing equations are solved for a filtered velocity field – representing the larger/grid scale flow motions. Meanwhile, the influence of the smaller/sub-grid scale (SGS) motions is represented by a model included in the filtered NS-equations. Thus, extensive calculations are avoided to explicitly solve the smaller-scale motions. Compared to RANS, LES has the advantage of describing the unsteady, grid-scale turbulent structures though it is computationally more expensive. Hence, it is a good choice to apply LES for solving the unsteady motion in turbulent flows to a certain extent of accuracy.

The earliest and simplest LES model was proposed by Smagorinsky [1], where the sub-grid scale (SGS) turbulent stress tensor is related to the resolved strain-rate tensor by a scalar eddy viscosity with a linear algebraic equation. Based on the linear eddy-viscosity assumption in the Smagorinsky model, more models are proposed by other researchers, including dynamic models [2–4], dynamic mixed models [5, 6], structure function models [7, 8], wall adapting local eddy viscosity model (WALE) [9], etc. More recently, the anisotropic minimum-dissipation (AMD) model has been proposed by Rozema et al. [10] and evaluated in OpenFOAM by Zahiri and Roohi [11, 12], which considers the effect of various directions in computing sub-grid stress and is capable of operating in transitional flows. In the above models, either constant model coefficient or dynamic model coefficient is adopted–an operation called test filtering is commonly used to evaluate the dynamic coefficient. Transport-equation model is another important LES approach, where transportation equations for the SGS terms are formulated, accounting for the historic and non-local effect of SGS kinetic energy due to production, dissipation and diffusion. Representative works on the transport-equation LES model are given by Deardorff [13], Schumann [14], Yoshizawa and Horiuti [15], Ghosal et al. [16], Fureby et al. [17], Krajnović and Davidson [18], Gallerano et al. [19]. The SGS turbulent stress tensor is explicitly modelled in the above introduced models, while Boris et al. [20] advocated to solve the filtered NS-equations without using an explicit SGS model and to use the inherent dissipation from the discretization scheme as an implicit SGS model. This approach is known as MILES (Monotone Integrated Large Eddy Simulation). Other representative LES calculations with this approach can be found in the studies by Tamura and Kuwahara [21], Knight et al. [22], Urbin and Knight [23]. The reader may refer to Meneveau and Katz [24], Pope [25], Yang [26] for more details about LES modelling, where the performance of various models is evaluated and discussed.

Although substantial efforts have been made to develop various SGS models in the last few decades, they all have limitations–a model which works very well for one type of problem may turn out to be unsuitable for another type of problem. In addition, the accurate simulation of near-wall flow regions is essential in many practical engineering

configurations, while it would become very expensive to perform a wall-resolved LES for turbulent flows with high Reynolds numbers [25]. Comprehensive reviews on wall layer modelling were provided by Piomelli and Balaras [27] and Piomelli [28], where it was pointed out that "no universally accepted model has appeared". Hence, it remains a challenge to resolve the near-wall regions accurately in LES nowadays. Consistent results can be achieved for DNS at various Reynolds numbers if the mesh size is comparable to the famous Kolmogorov lengthscale ($\eta \sim \text{Re}^{-3/4}$), where Re is the Reynolds number defined by the bulk flow velocity). However, it is difficult to find out the appropriate mesh configurations in LES to get consistent results that scale reasonably with Reynolds number. This usually becomes very tedious when simulations need to be conducted for various Reynolds numbers, as the results of the LES are sensitive to the mesh size even for a fixed Reynolds number [29]. In this paper, a scaling law relating the mesh size to the Reynolds number was proposed to ensure consistent results for LES as the Reynolds number was varied, where the scaling law was further verified in the plane channel flow simulation.

2   Governing equations and numerical methods

In this section, the governing equations for LES, the SGS modelling, as well as the numerical schemes are introduced. In the present work, simulations are performed with an open source CFD tool, OpenFOAM, which provides a large variety of solvers, discretization schemes and turbulence models, as well as the flexibility of developing new libraries according to the users' need. The self-developed code in OpenFOAM also possesses the capability of processing the data in parallel using the message passing interface (MPI) mechanism.

2.1   Governing equations and LES turbulence modelling

The incompressible flow of Newtonian fluids is governed by the continuity equation (2.1a) and Navier-Stokes equations (2.1b) shown as follows (in Cartesian tensor notation),

$$\begin{cases} \dfrac{\partial U_i}{\partial x_i}=0, & \text{(2.1a)} \\[2mm] \dfrac{\partial U_j}{\partial t}+\dfrac{\partial U_i U_j}{\partial x_i}=\nu\dfrac{\partial^2 U_j}{\partial x_i\partial x_i}-\dfrac{1}{\rho}\dfrac{\partial p}{\partial x_j}, & \text{(2.1b)} \end{cases}$$

where U_i (or $\mathbf{U}$ in vector notation) and p denote the fluid velocity and pressure, respectively, and ρ and ν represent the fluid density and kinematic viscosity, respectively. The above equations can be solved using a very fine mesh for all scales of motions, i.e., using direct numerical simulation (DNS). However, the computational cost of DNS is too high, and it is thus inapplicable for practical high-Reynolds-number flows. Most of the computational effort in DNS is on the small dissipative motions, whereas the energy and

anisotropy are contained predominantly in the larger scales of motion [25]. Hence in LES, the dynamics of the larger-scale motions are computed explicitly, the influence of the smaller scales being represented by simple models. To achieve that, the velocity **U** is decomposed into the sum of a filtered/resolved component $\overline{\mathbf{U}}$ (representing the grid-scale motions) and a subgrid-scale (SGS) component **u** by a spatial filtering operation. The filtered conservation equations can thus be obtained from Eq. (2.1) as follows,

$$\begin{cases} \dfrac{\partial \bar{U}_i}{\partial x_i} = 0, & (2.2a) \\[4mm] \dfrac{\partial \bar{U}_j}{\partial t} + \dfrac{\partial \bar{U}_i \bar{U}_j}{\partial x_i} = \nu \dfrac{\partial^2 \bar{U}_j}{\partial x_i \partial x_i} - \dfrac{1}{\rho} \dfrac{\partial \tilde{p}}{\partial x_j} - \dfrac{\partial \tau_{ij}^D}{\partial x_i}, & (2.2b) \end{cases}$$

where the SGS stress tensor is defined as $\tau_{ij} = \tau_{ji} = \overline{U_i U_j} - \bar{U}_i \bar{U}_j$. The SGS kinetic energy and the deviatoric SGS stress tensor are defined as

$$k_{sgs} = \frac{1}{2} \tau_{ii} \quad \text{and} \quad \tau_{ij}^D = \tau_{ij} - \frac{1}{3} \tau_{kk} \delta_{ij} = \tau_{ij} - \frac{2}{3} k_{sgs} \delta_{ij}.$$

The SGS kinetic energy is subsumed into a modified filtered pressure $\tilde{p} = \bar{p} + \frac{2}{3} \rho k_{sgs}$ [25].

Turbulence (closure) modelling for τ_{ij}^D is required to close the above system of equations, and various LES models are available nowadays. As was mentioned previously, there is not a universally accepted LES model that has been proven to be applicable for all practical flows; and more complicated models do not necessarily guarantee better performance [27, 28]. More importantly, a sufficiently fine mesh is still required to capture most of the turbulent kinetic energy in current wall-resolved LES and the LES model only takes care of the sub-grid-scale turbulent motion. Hence, we have chosen the most fundamental and widely used LES model for current study, i.e., the Smagorinsky model. The SGS stress tensor τ_{ij}^D is related to the filtered rate-of-strain tensor,

$$\bar{S}_{ij} = \frac{1}{2} \left(\frac{\partial \bar{U}_i}{\partial x_j} + \frac{\partial \bar{U}_j}{\partial x_i} \right),$$

through the eddy viscosity (ν_t), i.e.,

$$\tau_{ij}^D = -2 \nu_t \bar{S}_{ij} = -\nu_t \left(\frac{\partial \bar{U}_i}{\partial x_j} + \frac{\partial \bar{U}_j}{\partial x_i} \right).$$

The eddy viscosity is calculated as $\nu_t = C_s^2 \Delta^2 \bar{S}$, where C_s is a dimensionless constant, Δ is the filter (grid) size and $\bar{S} = \sqrt{2 \bar{S}_{ij} \bar{S}_{ij}}$ is defined as the characteristic filtered rate-of-strain. Lilly [30] derived $C_s \approx 0.17$ from homogeneous isotropic turbulence, while it was found to be too dissipative. It has been shown that $C_s \approx 0.1$ behaves reasonably well in turbulent channel flow [8, 31, 32] and this value is used in current study. The standard Smagorinsky model tends to overestimate the wall shear stress due to non-zero

eddy viscosity at the wall. To achieve satisfactory simulation accuracy with the standard Smagorinsky model, we need to apply very fine mesh in the near wall viscous region to reduce the eddy viscosity, which will increase the computational time significantly. The Van-Driest-type damping function [33] is used for the filter width to ensure negligible eddy viscosity near a wall, as has been widely applied in many other studies, including Moin and Kim [32], Piomelli [34], Lenormand [35] and others. The damping function is supposed to suppress the turbulence modelling in the near-wall region by reducing the filter width, so that most of the turbulent kinetic energy and Reynolds stresses are carried by the grid-scale motions and the near-wall region is resolved in a manner similar to that of direct numerical simulation (DNS). Hence, a sufficiently fine mesh is still required to capture most of the turbulent activities in current wall-resolved LES. With the SGS stress tensor (τ_{ij}^D) modelled, the momentum equation (2.2b) can be further written as follows in both tensor notation and vector notation,

$$\begin{cases} \dfrac{\partial \bar{U}_j}{\partial t} + \dfrac{\partial \bar{U}_i \bar{U}_j}{\partial x_i} - \dfrac{\partial}{\partial x_i}\left(\nu_{eff}\dfrac{\partial \bar{U}_j}{\partial x_i}\right) - \dfrac{\partial}{\partial x_i}\left(\nu_{eff}\dfrac{\partial \bar{U}_i}{\partial x_j}\right) + \dfrac{1}{\rho}\dfrac{\partial \tilde{p}}{\partial x_j} = G\delta_{xj}, \\[4mm] \dfrac{\partial \bar{\mathbf{U}}}{\partial t} + \nabla\cdot(\bar{\mathbf{U}}\bar{\mathbf{U}}) - \nabla\cdot\left(\nu_{eff}\nabla\bar{\mathbf{U}}\right) - \nabla\cdot\left[\nu_{eff}(\nabla\bar{\mathbf{U}})^T\right] + \dfrac{1}{\rho}\nabla\tilde{p} = G\mathbf{i}, \end{cases} \tag{2.3}$$

where the effective viscosity is defined as $\nu_{eff} = \nu + \nu_t$. For experiments, a very long physical channel is required to allow the flow to become fully turbulent. However, for numerical simulations, a long channel is not realistic due to the huge computational costs. Hence, a constant pressure gradient (normalized by ρ and denoted as G in Eq. (2.3)) is added in the longitudinal direction (x-direction) and periodic boundary conditions are applied for the channel inlet and outlet. Similarly, periodic boundary conditions are also applied along the spanwise direction (z-direction) for the left and right domain boundaries. Lastly, the no-slip condition is applied along the top and bottom walls (corresponding to the wall-normal y-direction). In this way, the flow is driven by the prescribed pressure gradient and becomes fully turbulent given a sufficiently long simulation time.

2.2 Numerical schemes

In OpenFOAM, the governing equations are solved with the finite volume method (FVM). In the present study, a second-order implicit backward scheme is applied for the temporal discretization ($\frac{\partial \bar{\mathbf{U}}}{\partial t}$). Standard finite volume discretization of Gaussian integration (Gauss scheme) is applied for the gradient terms ($\nabla\bar{\mathbf{U}}$ and $\nabla\tilde{p}$). Second-order Gauss central-differential scheme is applied for the discretization of divergence terms, including the velocity advection term ($\nabla\cdot(\bar{\mathbf{U}}\bar{\mathbf{U}})$) and another diffusive term ($\nabla\cdot[\nu_{eff}(\nabla\bar{\mathbf{U}})^T]$). Gauss scheme is applied for the Laplacian term ($\nabla\cdot(\nu_{eff}\nabla\bar{\mathbf{U}})$), where the surface normal gradient ($\mathbf{n}\cdot\nabla\bar{\mathbf{U}}$) is discretized with second order accuracy. Lastly, second-order central-differential interpolation scheme was used to interpolate values from cell centres to face centres. The discretized equations are solved iteratively with the Pressure-Implicit with Splitting of Operators (PISO) algorithm, which is a popular numerical

scheme for pressure-velocity coupled equations. Large linear equation systems (in the form of $\mathbf{Ax}=\mathbf{b}$) are derived when the governing equations are discretized on all computation cells. $\mathbf{A}$ is a sparse matrix containing the coefficients of the spatial discretization. Vector $\mathbf{x}$ stores the values of velocity or pressure, the dimension of which is the total number of computation cells. Vector b stores the explicitly calculated flow data and the boundary information. The linear equation system for the velocity is solved by Gauss-Seidel smooth solver and Geometric-algebraic multi-grid (GAMG) solver is applied to the linear equation system for the pressure. The implementation of the above numerical schemes in OpenFOAM requires lengthy descriptions, and interested readers may refer to Appendix A for more details.

3 A mesh size scaling law with Reynolds number

In the current study, we attempt to apply the LES to a plane channel flow with the near-wall region well-resolved and to obtain consistent results over a range of Reynolds numbers ($\mathrm{Re}_\tau=395,590,1000$). Hence, a mesh size scaling law with Reynolds number becomes essential. For the current simulations for a channel flow, a uniform mesh is applied along the streamwise ($x-$) and spanwise ($z-$) direction–both are homogeneous, while hyperbolic distribution of nodes is adopted in the wall normal ($y-$) direction for generating a very fine mesh near the wall and a coarser mesh in the vicinity of the channel centreline. Hence, the mesh interval along the $x-$ and $z-$ directions can be determined as

$$\Delta x = L_x/(N_x-1) \quad \text{and} \quad \Delta z = L_z/(N_z-1),$$

where L_x and L_z are the streamwise length and spanwise width of the computation domain; and N_x and N_z are the number of grid points on the respective edges. The node distribution in the wall normal direction is symmetric about the channel centreline and follows the hyperbolic function shown as follows:

$$\begin{cases} \sinh b = \dfrac{L_y}{(N_y-1)\Delta y_w}b, & (\text{solve numerically for } b>0), \\[2mm] S_i = \dfrac{L_y}{2}\left[1+\dfrac{\tanh(\frac{i-1}{N_y-1}b-\frac{1}{2}b)}{\tanh\frac{b}{2}}\right], & \left(1\leq i\leq N_y\right), \\[2mm] \Delta y_i = S_{i+1}-S_i, & \left(1\leq i\leq N_y-1\right), \end{cases} \tag{3.1}$$

where Δy_w is the mesh interval in the wall-normal direction at the wall and i denotes the index of the nodes. It can be verified that $\Delta y_1 = \Delta y_{N_y-1} = \Delta y_w$ as shown in the following:

$$\begin{cases} \Delta y_1 = \dfrac{L_y}{2}\left[1+\dfrac{\tanh\left(\frac{b}{N_y-1}-\frac{b}{2}\right)}{\tanh\frac{b}{2}}\right] \approx \dfrac{L_y}{2}\left[1+\dfrac{\tanh\left(-\frac{b}{2}\right)+\frac{b}{N_y-1}\tanh'\left(-\frac{b}{2}\right)}{\tanh\frac{b}{2}}\right] \\[3mm] \qquad = \dfrac{L_y}{2}\left[\dfrac{\Delta y_w\sinh b}{L_y}\dfrac{1-\tanh^2\left(\frac{b}{2}\right)}{\tanh\frac{b}{2}}\right] = \Delta y_w\cosh^2\left(\dfrac{b}{2}\right)\left[1-\tanh^2\left(\dfrac{b}{2}\right)\right] = \Delta y_w, \\[3mm] \Delta y_{N_y-1} = L_y - \dfrac{L_y}{2}\left[1+\dfrac{\tanh\left(\frac{b}{2}-\frac{b}{N_y-1}\right)}{\tanh\frac{b}{2}}\right] \approx \dfrac{L_y}{2}\left[1-\dfrac{\tanh\left(\frac{b}{2}\right)-\frac{b}{N_y-1}\tanh'\left(\frac{b}{2}\right)}{\tanh\frac{b}{2}}\right] \\[3mm] \qquad = \dfrac{L_y}{2}\left[\dfrac{\Delta y_w\sinh b}{L_y}\dfrac{1-\tanh^2\left(\frac{b}{2}\right)}{\tanh\frac{b}{2}}\right] = \Delta y_w. \end{cases}$$

Assuming that N_y is an odd number, we can find out the node interval size in the wall normal direction at the channel centreline as follows:

$$\Delta y_c = S_{\frac{N_y+1}{2}} - S_{\frac{N_y-1}{2}} = \dfrac{L_y}{2} - \dfrac{L_y}{2}\left[1+\dfrac{\tanh\left(-\frac{b}{N_y-1}\right)}{\tanh\frac{b}{2}}\right] = \dfrac{L_y\tanh\left(\frac{b}{N_y-1}\right)}{2\tanh\frac{b}{2}}.$$

In practice, we have $N_y > 100$, $\Delta y_w^+ \sim \mathcal{O}(0.1)$ and thus

$$\dfrac{L_y}{(N_y-1)\Delta y_w} = \dfrac{2\mathrm{Re}_\tau}{(N_y-1)\Delta y_w^+} \sim \mathcal{O}(10),$$

$b > 4$. Considering that the difference between $\sinh(4)$ and $\cosh(4)$ is less than 0.07%, the following approximation can be made with a very small discrepancy

$$\begin{cases} \tanh\left(\dfrac{b}{N_y-1}\right) \approx \dfrac{b}{N_y-1}, \\[3mm] \dfrac{L_y}{(N_y-1)\Delta y_w}b = \sinh b \approx \cosh b \approx 0.5e^b. \end{cases}$$

Hence, we can estimate Δy_c with good accuracy as follows:

$$\Delta y_c \approx \dfrac{L_y}{2\tanh\frac{b}{2}}\dfrac{b}{N_y-1} = \dfrac{L_y}{2\tanh\frac{b}{2}}\dfrac{\Delta y_w\sinh b}{L_y} = \Delta y_w\dfrac{1+\cosh b}{2} \approx \dfrac{e^b}{4}\Delta y_w.$$

If we have specified the ratio between the wall mesh size and the channel centreline mesh size, i.e., $\frac{\Delta y_c}{\Delta y_w}$, the value of b can be obtained as $b \approx \ln(4\frac{\Delta y_c}{\Delta y_w})$. The number of nodes in the wall-normal direction can thus be determined as

$$N_y - 1 \approx \dfrac{L_y}{2\Delta y_c}\ln\left(4\dfrac{\Delta y_c}{\Delta y_w}\right).$$

We have thus determined the explicit relation between the mesh interval and number of nodes required in all three dimensions, as shown in Eq. (3.2):

$$\begin{cases} N_x - 1 = L_x / \Delta x, \\ N_z - 1 = L_z / \Delta z, \\ N_y - 1 = \dfrac{L_y}{2\Delta y_c} \ln\left(4\dfrac{\Delta y_c}{\Delta y_w}\right). \end{cases} \tag{3.2}$$

The actual mesh size would vary greatly as the Reynolds number changes. However, the variation is much smaller if we measure the interval size using viscous scales (wall or inner units). The viscous scales are obtained as follows:

$$\begin{cases} u_\tau = \sqrt{\tau_w / \rho} = \sqrt{\delta G}, \\ \delta_v = v / u_\tau, \\ \mathrm{Re}_\tau = u_\tau \delta / v = \delta / \delta_v, \end{cases}$$

where δ is the half-channel height, τ_w is the wall shear stress, u_τ is the friction velocity, δ_v is the viscous length scale and G is the prescribed streamwise pressure gradient in Eq. (2.3). Eq. (3.2) can thus be written as follows:

$$\begin{cases} N_x - 1 = \dfrac{L_x}{\delta} \dfrac{\mathrm{Re}_\tau}{\Delta x^+}, \\ N_z - 1 = \dfrac{L_z}{\delta} \dfrac{\mathrm{Re}_\tau}{\Delta z^+}, \\ N_y - 1 = \dfrac{\mathrm{Re}_\tau}{\Delta y_c^+} \ln\left(4\dfrac{\Delta y_c^+}{\Delta y_w^+}\right). \end{cases} \tag{3.3}$$

If Δx^+, Δz^+, Δy_w^+, Δy_c^+ are all constants, the total number of grid points $N_{xyz} = N_x N_y N_z$ scales with the friction Reynolds number as $N_{xyz} \sim \mathrm{Re}_\tau^3$. According to the empirical law of $\mathrm{Re}_\tau \approx 0.09\mathrm{Re}^{0.88}$ for a channel flow [25], we have $N_{xyz} \sim \mathrm{Re}^{2.64}$. Such a scaling exponent of 2.64 is even larger than that for DNS ($N_{xyz} \sim \mathrm{Re}^{9/4}$), which is apparently unrealistic for LES. By integrating the model energy spectrum function, Pope [25] proposed that 90% of the turbulent kinetic energy is contained by the motions of lengthscales larger than $0.16L_{11}$, where L_{11} is an integral lengthscale obtained by integrating the longitudinal autocorrelation function. He further showed that L_{11} tends to be linearly related to another lengthscale L ($L_{11} \approx 0.43L$) in turbulent flows with sufficiently high Reynolds number. The lengthscale L characterizes the large eddies in turbulent flows and is defined as $L = k^{1.5}/\varepsilon$, where k is the turbulent kinetic energy and ε is the dissipation rate. Thanks to the rapid development of computing power, abundant DNS data is available for investigating the relation between L and the Reynolds number nowadays. In this current study, the DNS results from Moser et al. [36] and Lee and Moser [37] are used for analysis. The variation of L in the wall-normal direction is plotted in Fig. 1(a), where inner units are adopted since the current LES aims for reasonably good resolution of the
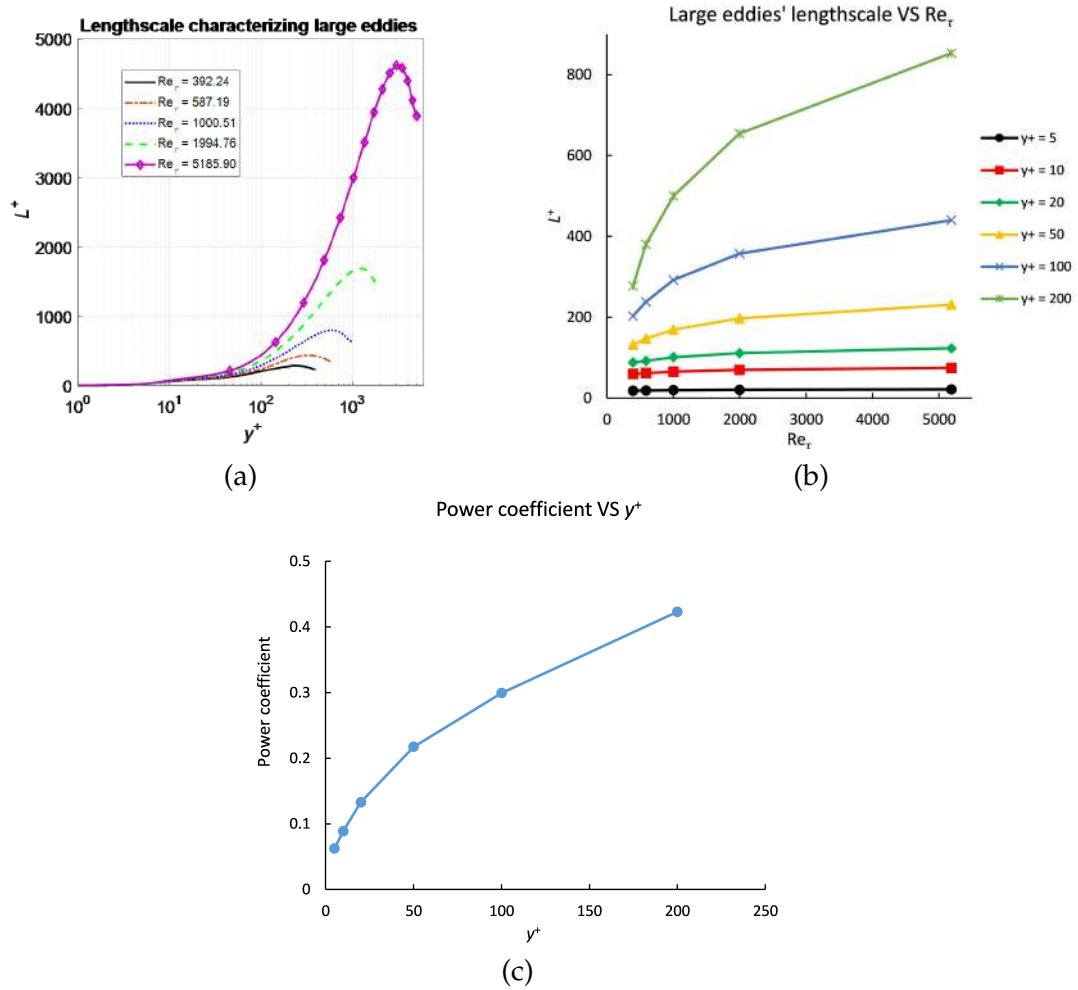
(a)

(b)

(c)

Figure 1: Variation of the lengthscale (L^+) characterizing the large eddies in turbulent flows. (a) shows the variation of L^+ with y^+ at different Reynolds numbers, (b) shows the variation of L^+ with Re_τ at different wall-normal distances and (c) shows the variation of the power coefficient C with y^+. The DNS results are from Moser et al. [36] and Lee and Moser [37].

near-wall region. It can be found that the variation of L with Reynolds number is much smaller in the near-wall region ($y^+ < 100$) compared to that near the channel centreline ($y^+/\mathrm{Re}_\tau > 0.5$). The variation of L^+ is further compared at different values of y^+ in Fig. 1(b). It may be seen that the lengthscale L^+ does not vary much near the wall and the dependence on Reynolds number only becomes significant for $y^+ > 50$. L^+ grows as the Reynolds number increases, but at a rate that is slower than that for a linear growth. It is thus reasonable to represent the relationship between L^+ and Re_τ as a power function $L^+ \sim \mathrm{Re}_\tau^C$, where $C < 1$ is the power coefficient.

The power coefficient C can be derived by fitting the curves in Fig. 1(b) with a power trendline and the results are shown in Fig. 1(c). It is found that the power coefficient C starts from a very small value near the wall and increases towards the channel centreline. Hence, the characteristic lengthscale L^+ increases with Reynolds number more rapidly nearer to the channel centreline. As discussed previously, 90% of the turbulent kinetic energy can be captured if the motions with lengthscales larger than $0.16 \times 0.43 L^+$ are resolved. We can thus conclude that a roughly fixed percentage (say 90%) of the turbulent kinetic energy can be resolved by LES if the mesh size varies linearly with L^+ as the Reynolds number changes. Since L^+ is almost independent of Reynolds number in the viscous sublayer ($C \approx 0$ for $y^+ < 5$), the same grid spacing needs to be maintained in the near-wall region in the wall normal direction, i.e., a constant Δy_w^+ for all Reynolds numbers. On the other hand, the mesh spacing dependency on the Reynolds number is more significant away from the wall ($y^+ > 5$) and we have Δy_c^+, Δx^+, $\Delta z^+ \sim L^+ \sim \mathrm{Re}_\tau^C$. Apparently, it is not realistic or necessary to vary Δy_c^+, Δx^+, Δz^+ with the distance from the wall, since Δy_c^+ represents the mesh size in the wall-normal direction at the channel centreline, and Δx^+, Δz^+ are uniform throughout the channel. For a fixed value of C, Δy_c^+, Δx^+, $\Delta z^+ \sim \mathrm{Re}_\tau^C$ actually represents a weighted relation for the whole channel according to the effect of different regions. Considering that all turbulent channel flows show a log-law region, we choose the values of C within that region. Hence, the selection of C is arbitrary between 0.2 and 0.35, corresponding to the values of C for $40 < y^+ < 150$, which is a common log-law region for flows with $\mathrm{Re}_\tau \geq 395$. A smaller C value indicates a weaker mesh size dependency on Reynolds number, suggesting a finer mesh configuration and more turbulent kinetic energy resolved. A larger C value corresponds to a coarser mesh configuration and less turbulent kinetic energy resolved. For this current study, we have adopted $C = 0.3$ as a good compromise and the scaling of Δx^+, Δz^+, Δy_c^+ with Re_τ can thus be prescribed as

$$\Delta x^+ = a_x \mathrm{Re}_\tau^{0.3}, \quad \Delta z^+ = a_z \mathrm{Re}_\tau^{0.3} \quad \text{and} \quad \Delta y_c^+ = a_y \mathrm{Re}_\tau^{0.3},$$

where a_x, a_z and a_y are constant coefficients. The relation between the number of nodes and the Reynolds number can thus be determined as follows:

$$\begin{cases} N_x - 1 = \dfrac{L_x}{\delta} \dfrac{\mathrm{Re}_\tau^{0.7}}{a_x}, \\[2mm] N_z - 1 = \dfrac{L_z}{\delta} \dfrac{\mathrm{Re}_\tau^{0.7}}{a_z}, \\[2mm] N_y - 1 = \dfrac{\mathrm{Re}_\tau^{0.7}}{a_y} \left[\ln\left(\dfrac{4 a_y}{\Delta y_w^+} \right) + 0.3 \ln \mathrm{Re}_\tau \right]. \end{cases} \tag{3.4}$$

The effect of $0.3 \ln \mathrm{Re}_\tau$ in Eq. (3.4) is not important for the Reynolds numbers in the present paper, which is subsumed by the much larger term $\ln(\frac{4 a_y}{\Delta y_w^+})$. Hence, we are able to derive the scaling relation between the number of grid nodes and the Reynolds number

as $N_{xyz} \sim \mathrm{Re}_\tau^{2.1} \sim \mathrm{Re}^{1.85}$. This is consistent to the estimation by Chapman [38] for LES in aerodynamic applications, where N_{xyz} scales with $\mathrm{Re}^{1.8}$. For the current study, the computational domain size is fixed as $L_x = 2\pi\delta$ and $L_z = \pi\delta$ for all numerical simulations at different Reynolds numbers, where δ is the half-channel height. Lozano-Duran and Jimenez [39] have shown that further increasing the domain size does not show significant advantage for Reynolds numbers up to $\mathrm{Re}_\tau = 4200$.

4 Simulation and discussion

In this section, the mesh-size scaling law introduced in the preceding section is validated with LES of channel flow at different Reynolds numbers. The simulation results are discussed and verified against published data.

4.1 Mesh configuration

In most DNS studies of channel flow [36,37,39,40] the mesh resolution in the wall-parallel directions is $\Delta x^+ \approx 10$ (streamwise) and $\Delta z^+ \approx 6$ (spanwise), which does not show obvious dependence on the Reynolds number. However, large variations are noted for the mesh spacing in the wall-normal direction among different studies, where Δy_w^+ varies from 0.01 to 0.5 and Δy_c^+ varies from 3.4 to 12.5. Though the mesh requirement is not as strict as DNS, a relatively fine mesh is still required in LES to resolve the near-wall region with a reasonable accuracy. In this section, the mesh size is varied at $\mathrm{Re}_\tau = 395$ to determine how the LES results would be affected. In the current LES study, the mesh spacing is kept in the same order of magnitude as that used in DNS studies though the overall mesh is coarser. The SGS turbulence modelling used in LES is expected to resolve the flow field on a coarser mesh with reasonable accuracy and to reduce the computational cost significantly. $\Delta y_w^+ = 0.2$ is applied for all LES studies in this paper to yield sufficiently good near-wall resolution since the viscous sublayer does not vary much with the Reynolds number and needs to be resolved in nearly the same manner as DNS. Such a wall boundary resolution is better than the suggested value ($0.5 \leq \Delta y_w^+ \leq 2$) in wall-resolved LES [29], and is quite close to that in some DNS studies. In that case, the damping function is applied to prevent excessive turbulent modelling near the wall, which was explained in Section 2.1. The SGS turbulence modelling used in LES is expected to resolve the flow field on a coarser mesh with reasonable accuracy and to reduce the computational cost significantly compared to DNS. Meanwhile, the time step size is selected to be sufficiently small so that the average CFL number is below 0.2 and the maximum CFL number is below 0.6. The complete parameters of the mesh configuration can be referred to in Table 1. The simulation time of the three LES cases was at least $Tu_\tau/\delta = 80$ for the flow to become stable, which is much longer than the time used in most DNS studies ($Tu_\tau/\delta \approx 10$). The simulation running time is around 1 week (48 CPU cores) at $\mathrm{Re}_\tau = 395$, 1 month (72 CPU cores) at $\mathrm{Re}_\tau = 590$ and 4 months (120 CPU cores) at $\mathrm{Re}_\tau = 1000$.

Table 1: Mesh configurations at $\mathrm{Re}_\tau = 395$.

Name	Δx^+	Δz^+	Δy_c^+	N_x	N_z	N_y
Re395F	19.1	15.5	18.2	131	81	131
Re395	16.5	12.4	15.3	151	101	151
Re395M	14.6	10.3	13.1	171	121	171

Table 2: Parameters at all Reynolds numbers in the present study. The bulk Reynolds number is defined as $\mathrm{Re} = (2\delta U_b)/\nu$ and the bulk velocity U_b is calculated as the quotient of the mean volume flow rate and the channel cross section area.

Name	Re_τ	Re	Δx^+	Δz^+	Δy_c^+	N_x	N_z	N_y	Tu_τ/δ	κ	B
Re395	394.97	13950	16.5	12.4	15.3	151	101	151	200	0.399	5.19
Re590	589.92	21990	14.6	14.3	17.3	201	131	201	140	0.396	4.97
Re1000	1000.00	40090	21.7	16.5	20.1	291	191	301	80	0.397	5.01

The mean streamwise velocity profiles determined by LES with the above mesh configurations are plotted and compared with the DNS result from Moser et al. [36] in Fig. 2. It can be found that the velocity profile deviates from the DNS data a lot if the LES model is turned off with the mesh configuration "Re395". On the other hand, the results from LES match fairly well with those from DNS throughout the whole channel for all three LES cases. In general, more accurate results are obtained with a finer mesh (more computation nodes) in LES. The deviation from DNS results is apparently larger in the case "Re395F" with fewer computational nodes and larger mesh spacings, especially in the channel centreline region ($y^+ > 0.3Re_\tau$). Nevertheless, the improvement of case "Re395M" compared to case "Re395" is already marginal, which implies that a 54% increase in the mesh nodes hardly improves the simulation results. Hence, the mesh configuration "Re395" shows a good balance between numerical accuracy and computational cost at $\mathrm{Re}_\tau = 395$; and it may thus be used to determine the mesh configurations at even higher Reynolds numbers with the help of the mesh size scaling law introduced in the preceding section. The values of ax, az and ay can be determined from the mesh configuration at $\mathrm{Re}_\tau = 395$ as follows, as well as the scaling relation between mesh size and Reynolds number:

$$\begin{cases} \Delta x^+ = a_x \mathrm{Re}_\tau^{0.3} \approx 2.7 \mathrm{Re}_\tau^{0.3}, \\ \Delta z^+ = a_z \mathrm{Re}_\tau^{0.3} \approx 2.1 \mathrm{Re}_\tau^{0.3}, \\ \Delta y_c^+ = a_y \mathrm{Re}_\tau^{0.3} \approx 2.5 \mathrm{Re}_\tau^{0.3}. \end{cases} \tag{4.1}$$

Simulations were conducted for higher Reynolds numbers at $\mathrm{Re}_\tau = 590$ and 1000, where the mesh size and number are determined with the scaling law introduced in Section 3. The coefficients have been calculated in Eq. (4.1) with the mesh configuration at $\mathrm{Re}_\tau = 395$. The values of a_x, a_z and a_y are maintained at approximately 2.7, 2.1 and 2.5, respectively, for the mesh configurations at $\mathrm{Re}_\tau = 590$ and 1000. The complete mesh parameters in the current study are summarized in Table 2, and the comparison with the theoretical values
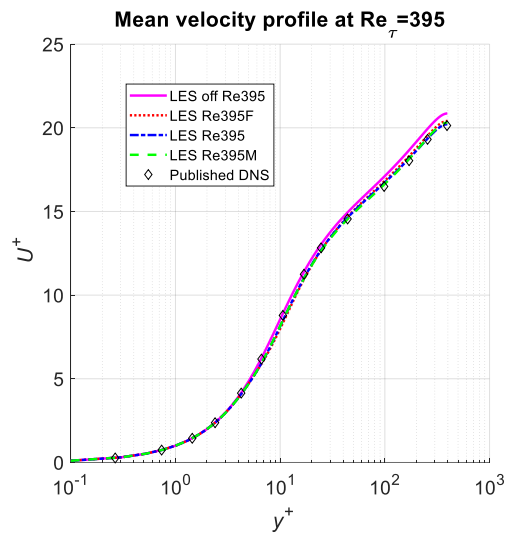
Figure 2: Mean streamwise velocity profile for $Re_\tau = 395$ with different mesh configurations. The DNS result is from Moser et al. [36].
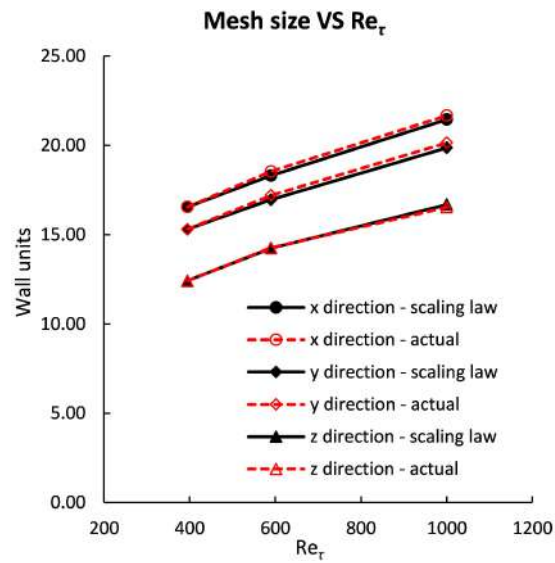

Figure 3: Comparison of the theoretical mesh size given by Eq. (4.1) and the actual mesh size in Table 2. Uniform mesh size is used in x and z directions, the y direction shows the mesh size at the channel centre.

given by Eq. (4.1) is shown in Fig. 3. It can be seen that the adopted mesh size follows the scaling relation very well.

4.2 Mean velocity

The mean streamwise velocity profiles are plotted in Fig. 4 for the data sets listed in Table 2. By fulfilling the mesh size scaling law, it can be found that consistent results are obtained as the Reynolds number (Re_τ) increases from 395 to 1000–good agreement with the DNS result throughout the whole channel. This verifies that the mesh size scaling relation introduced in Section 3 is capable of ensuring consistent results as the Reynolds number varies. Fig. 4 also shows that the velocity profiles at different Reynolds numbers collapse well onto a common trend line in the log law region, whose extent increases with Re_τ. The log-law relation is written as follows,

$$U^+ = \frac{1}{\kappa}\ln y^+ + B, \tag{4.2}$$

where κ is the von Kármán constant and B is another constant. The values of κ and B were determined for all cases in Table 2 by fitting the mean velocity data from $50 < y^+ < 0.3 Re_\tau$ with $R^2 = 0.999$, where R^2 is the coefficient of determination ($R^2 = 1$ stands for a perfect fit). The values of κ and B show good consistency among various Reynolds numbers and are very close to those in the DNS studies [36,37], $\kappa = 0.399$ and $B = 5.02$ ($Re_\tau = 395$), $\kappa = 0.400$ and $B = 5.05$ ($Re_\tau = 590$), $\kappa = 0.397$ and $B = 4.86$ ($Re_\tau = 1000$). Meanwhile, the present values agree well with those suggested by Pope [25], which are 0.41 and 5.2 respectively; and those reported in the experiment by Schultz and Flack [41], $\kappa = 0.40$ and $B = 5.0$. Overall, the current LES gives a good prediction of the mean velocity profile for a channel flow and the grid size scaling law ensures consistent results as the Reynolds number varies.
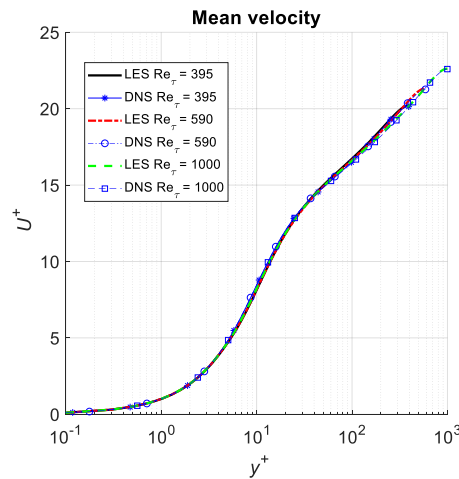

Figure 4: Comparison of the mean streamwise velocity profiles between LES and DNS at different Reynolds numbers. The DNS results at $Re_\tau = 395$ and 590 are from Moser et al. [36], and those at $Re_\tau = 1000$ are from Lee and Moser [37].

4.3　Shear stress and Reynolds stress

In a fully developed channel flow driven by a constant pressure gradient, the total shear stress (τ) follows a linear profile in the wall-normal (y) direction, which in both laminar and turbulent flows. The linear shear stress profile is given by Eq. (4.3)

$$\tau(y) = \tau_w \left(1 - \frac{y}{\delta}\right), \tag{4.3}$$

where $\tau_w = \tau(y=0)$ is the wall shear stress. For a turbulent flow, the total shear stress (τ) is the sum of the viscous shear stress ($\rho \nu \partial \langle U \rangle / \partial y$) and the Reynolds shear stress ($-\rho \langle uv \rangle$), where the terms with the angle brackets $\langle\ \rangle$ denote the time-mean values. In LES studies, an additional term ($-\langle \tau_{xy}^D \rangle$) is included in the total shear stress due to the SGS turbulence modelling. The composition of the total shear stress in the current LES can be derived by taking the time-mean of the x-momentum equation from Eq. (2.2b) as follows.

$$\rho \frac{\partial}{\partial y} \left[\nu \frac{\partial \langle \bar{U} \rangle}{\partial y} - \langle \bar{u}\bar{v} \rangle - \left\langle \tau_{xy}^D \right\rangle \right] = \frac{\partial \langle \tilde{p} \rangle}{\partial x}.$$

Since the mean pressure gradient along the x-direction is a prescribed constant, we have the total shear stress for LES shown in Eq. (4.4)

$$\tau = \rho \nu \frac{\partial \langle \bar{U} \rangle}{\partial y} - \rho \langle \bar{u}\bar{v} \rangle - \rho \left\langle \tau_{xy}^D \right\rangle, \tag{4.4}$$

where $\bar{u}$, $\bar{v}$ represent the fluctuation of the filtered velocity (e.g., $\bar{u} = \bar{U} - \langle \bar{U} \rangle$) and the SGS stress tensor τ_{ij}^D is calculated from the LES modelling (see Section 2.1 for details). In addition to the viscous shear stress and the grid-scale Reynolds shear stress, the total shear stress comprises another modelled stress, i.e., $-\rho \langle \tau_{xy}^D \rangle$. Profiles of the shear stresses are plotted in Figs. 5(a), (c) and (e), where linear variation of the total shear stress is obtained for all Reynolds numbers in the current study. It is apparent that the viscous shear stress dominates in the near-wall region but becomes negligibly small compared with the Reynolds shear stress as the distance from the wall increases. The peak of the grid-scale Reynolds shear stress increases with the Reynolds number, and so is the modelled shear stress. The modelled shear stress is mostly confined within a small region near the wall, for which its change is rapid, especially near the peak. It can be found that the small region is roughly between the range of $3 < y^+ < 10$ if the shear stresses are plotted using the wall viscous units. The rapid variation is because τ_{ij}^D largely depends on the local velocity gradient and the grid size, which show large variations in the near wall region.

　　The other non-zero components of the Reynolds stress tensor (i.e., $\langle \bar{u}^2 \rangle$, $\langle \bar{v}^2 \rangle$ and $\langle \bar{w}^2 \rangle$, where ρ is omitted for simplification) are shown in Figs. 5(b), (d) and (f), together with the comparison with DNS data. In generally, the above Reynolds normal stresses obtained by LES are lower than the DNS data. The current LES has predicted almost equal peaks for $\langle \bar{u}^2 \rangle$ compared to the published DNS data, and smaller peaks are captured by the
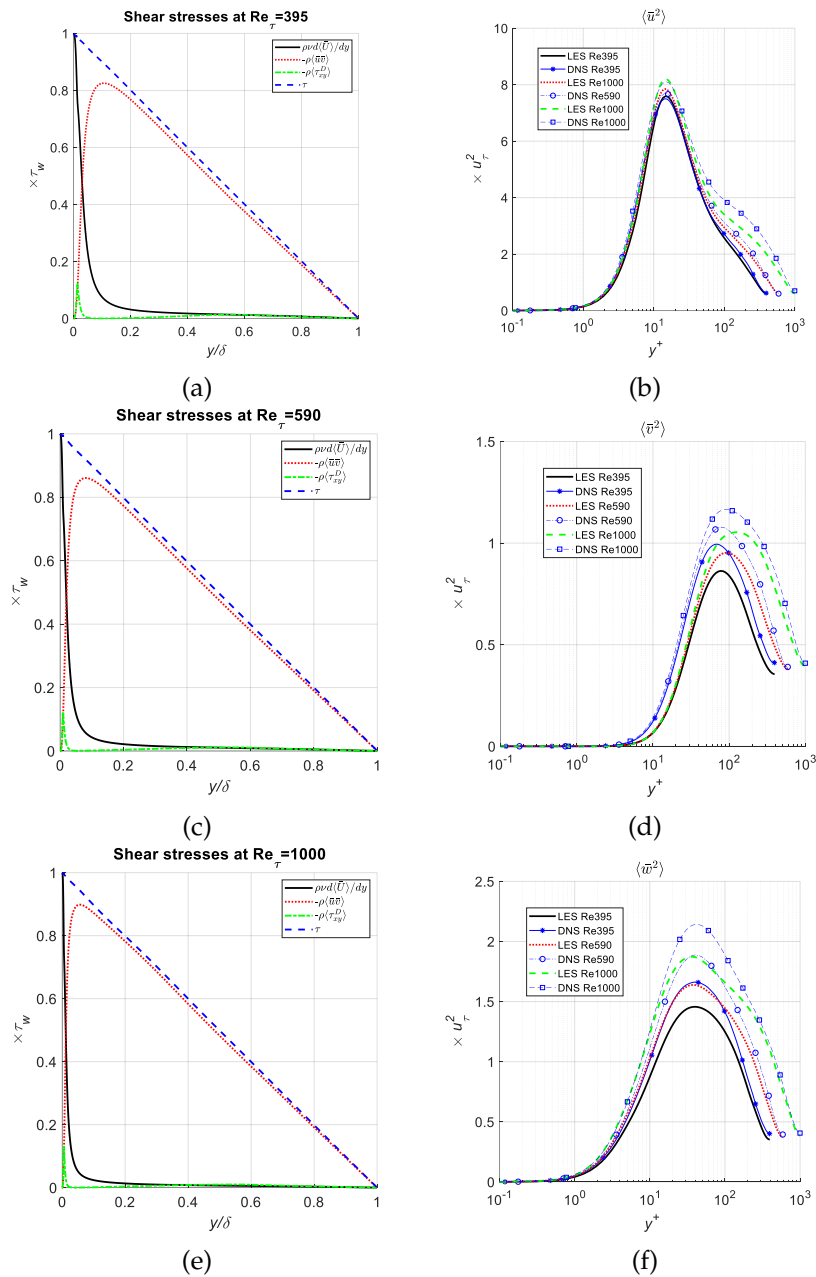
Figure 5: Shear stresses and Reynolds stresses. (a), (c) and (e) show the components of the total shear stress. (b), (d) and (f) show the profiles of Reynolds stress tensor ($\langle \bar{u}^2 \rangle$, $\langle \bar{v}^2 \rangle$ and $\langle \bar{w}^2 \rangle$) and the comparison with DNS result. The vertical axis tittles (x_{τ_ω} and $x_{u_\tau^2}$) are the multiplication of the wall shear stress and the square of the friction velocity, respectively. The DNS results at $Re_\tau = 395$ and 590 are from Moser et al. [36] and those at $Re_\tau = 1000$ are from Lee and Moser [37].

current LES for the other two components. Meanwhile, the locations of the peak values for LES are very close to those for DNS. The mismatch with DNS data is expected and is also reported in LES studies on channel flow by Lenormand et al. [35], Chatzikyriakou et al. [42], Kermani et al. [43] and others. The underestimation of the Reynolds stresses is not surprising, since LES is performed on a coarser mesh and the filtered velocity cannot contain as many fluctuations as the fully-resolved velocity in DNS. In addition, velocity fluctuations are further inhibited by the SGS turbulence modelling through the eddy viscosity v_t, which increases the effective flow viscosity and friction. Despite the above-mentioned discrepancy with the DNS data, the overall trend of the curves is the same as that in DNS at the same flow condition. More importantly, the variation of the curve with Reynolds number is consistent with that in DNS. Following the mesh scaling law, we can thus give reasonably good prediction to a flow with even higher Reynolds number at significantly lower computational cost.

4.4 Turbulent kinetic energy

The turbulent kinetic energy (TKE) in large eddy simulation consists of two parts, i.e., the grid-scale TKE and subgrid-scale TKE. The GS-TKE is calculated directly from the filtered/resolved flow field, while the SGS-TKE can only be modelled. The calculation of GS-TKE is the same as the TKE in DNS, i.e., $k_{gs} = \langle \bar{u}_i \bar{u}_i \rangle / 2$. In the Smagorinsky model, the assumption is made that the transfer rate of energy $(-\tau_{ij}^D \bar{S}_{ij})$ to the sub-grid motions is balanced by SGS dissipation (ε_{sgs}), which can thus be modelled as follows:

$$\varepsilon_{sgs} = \tau_{ij}^D \bar{S}_{ij} = -v_t \bar{S}^2 = -C_s^2 \Delta^2 \bar{S}^3. \tag{4.5}$$

The relation between the SGS dissipation and the SGS-TKE can be further modelled as

$$\varepsilon_{sgs} = -\frac{C_\varepsilon}{\Delta} k_{sgs}^{3/2},$$

which is commonly used in the model transport equation of SGS-TKE [15, 16, 19, 30]. Hence, the SGS-TKE can be determined as follows:

$$k_{sgs} = \left(-\frac{\Delta}{C_\varepsilon} \varepsilon_{sgs} \right)^{\frac{2}{3}} = C_s^{\frac{4}{3}} C_\varepsilon^{-\frac{2}{3}} \Delta^2 \bar{S}^2, \tag{4.6}$$

where $C_s \approx 0.1$ as discussed in Section 2.1, and $C_\varepsilon \approx 1$ as suggested by Lilly [30] and Yoshizawa and Horiuti [15], which have been adopted in current study. The variations of the GS-TKE and the SGS-TKE are shown in Figs. 6(a)-(c), as well as the comparison with DNS data. Comparison of the GS-TKE and the SGS-TKE clearly shows that current LES can resolve most of the turbulent kinetic energy in the grid scale. It can be found that the GS-TKE obtained by LES is generally smaller than the TKE in DNS and the peak locations are quite close for the two types of simulations. This is consistent with the results in Section 4.3, considering that the GS-TKE is calculated as

$$k_{gs} = \frac{1}{2} (\langle \bar{u}^2 \rangle + \langle \bar{v}^2 \rangle + \langle \bar{w}^2 \rangle).$$

The total TKE (GS+SGS) in LES matches with the TKE in DNS fairly well for all Reynolds numbers in the current study, especially in the near-wall region ($y^+ < 10$), where the total TKE is almost accurately predicted with the current LES configurations. In addition, the variation of the turbulent kinetic energy with Reynolds number is consistent with that for DNS, which verifies that the grid size scaling law is helpful for determining the appropriate mesh configuration so that roughly the same amount of turbulent kinetic energy can be resolved at different Reynolds numbers.

In the LES formulation, the TKE transport equation, which governs the evolution of the GS-TKE, is given by Eq. (4.7). Detailed derivation of the equation can be referred to in Appendix B

$$
\frac{\partial k_{gs}}{\partial t} + \langle \bar{U}_i \rangle \frac{\partial k_{gs}}{\partial x_i}
$$

$$
= \underbrace{-\langle \bar{u}_i \bar{u}_j \rangle \frac{\partial \langle \bar{U}_j \rangle}{\partial x_i}}_{\text{production } (\mathcal{P})} \underbrace{- \frac{1}{2} \frac{\partial \langle \bar{u}_i \bar{u}_j \bar{u}_j \rangle}{\partial x_i}}_{\text{turbulent transport}} \underbrace{+ \nu \frac{\partial^2 k_{gs}}{\partial x_i \partial x_i}}_{\text{viscous diffusion}} \underbrace{- \nu \left\langle \frac{\partial \bar{u}_j}{\partial x_i} \frac{\partial \bar{u}_j}{\partial x_i} \right\rangle}_{\text{dissipation } (\varepsilon)} \underbrace{- \frac{1}{\rho} \frac{\partial \langle \bar{u}_i \tilde{p}' \rangle}{\partial x_i}}_{\text{pressure transport}}
$$

$$
- \left\langle \bar{u}_j \frac{\partial \tau_{ij}^D}{\partial x_i} \right\rangle. \tag{4.7}
$$

The above formulation is different from the TKE transport equation in DNS, which can be found in Pope [25] and Lee and Moser [37]. In addition to the five named terms, we have one more term originating from the SGS stress tensor (τ_{ij}^D), which can be further decomposed into two terms as follows:

$$
- \left\langle \bar{u}_j \frac{\partial \tau_{ij}^D}{\partial x_i} \right\rangle = - \frac{\partial \langle \bar{u}_j \tau_{ij}^D \rangle}{\partial x_i} - \left(- \langle \tau_{ij}^D \bar{s}_{ij} \rangle \right),
$$

where $- \langle \tau_{ij}^D \bar{s}_{ij} \rangle$ is the fluctuational contribution of the entire mean kinetic energy transferred to the sub-grid-scale motions

$$
\left(- \langle \tau_{ij}^D \bar{S}_{ij} \rangle = - \langle \tau_{ij}^D \rangle \langle \bar{S}_{ij} \rangle - \langle \tau_{ij}^D \bar{s}_{ij} \rangle \right).
$$

Hence, it represents the kinetic energy loss from the grid-scale motion to the sub-grid-scale motion due to the grid-scale fluctuational flow motion. The other term, $-\partial \langle \bar{u}_j \tau_{ij}^D \rangle / \partial x_i$, has the same form as the transport terms in Eq. (4.7), which may thus be understood as the SGS stress transport. The balance of the TKE budget is calculated by summing up all the terms on the right-hand side of Eq. (4.7), which should theoretically be equal to zero under statistically stationary flow conditions. The balance of the TKE budget is plotted in Fig. 6(d), where the notation "w" denotes balance curves with the additional term in Eq. (4.7), while "w/o" indicates the curves without the additional term. Schiavo et al. [44] have also investigated the TKE budget in LES for a channel flow,
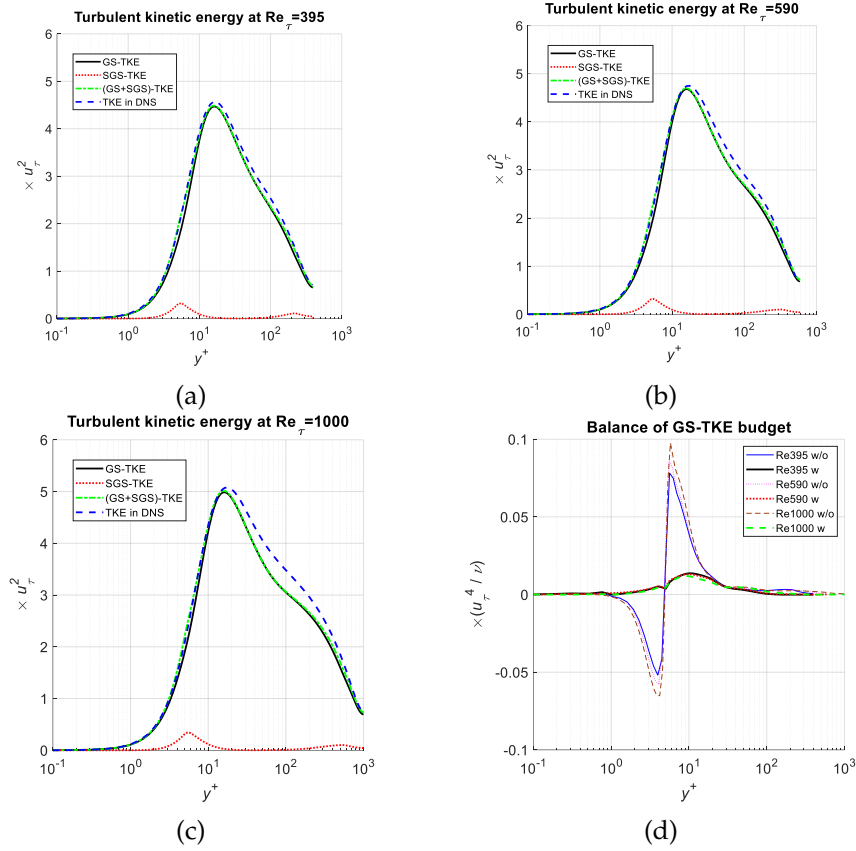
Figure 6: Turbulent kinetic energy and balance of TKE budget. (a), (b) and (c) show the variation of the turbulent kinetic energy (including GS-TKE, SGS-TKE and the summation) at different Reynolds numbers, as well as the comparison with DNS result. (d) shows the balance of the TKE budget in LES formulation. The DNS results at $Re_\tau = 395$ and 590 are from Moser et al. [36] and those at $Re_\tau = 1000$ are from Lee and Moser [37].

but did not consider the last term in Eq. (4.7). The variation of the balance curves obtained by them is of the same order of magnitude ($\sim 0.05 u_\tau^4/v$) as the curves without the additional term in Fig. 6(d). The balance curves are significantly improved when the additional term is taken into account. The maximum value of the balance is approximately $0.01 u_\tau^4/v$ and occurs near $y^+ = 10$, which is largely independent of the Reynolds number. The slightly numerical imbalance is induced by the limited resolution of the mesh as well as the rapid variation of the grid size and the velocity gradient near the wall. Furthermore, we may find that consistent results for the TKE budget balance can be obtained at different Reynolds numbers by satisfying the grid size scaling law.

4.5   Velocity spectra

Streamwise $(x-)$ one-dimensional spectral densities of the velocity fluctuations $(E_{uu}(\kappa_x),$ $E_{vv}(\kappa_x)$ and $E_{ww}(\kappa_x))$ are shown in Figs. 7-9, where κ_x represents the wavenumber in the streamwise direction. The current LES results are compared against the DNS results from literature [36, 37] at $Re_\tau = 395$, 590 and 1000; the velocity spectra are measured at two distances from the wall, i.e., $y^+ = 20$ and 40. It can be found from the comparison that the LES results match the DNS results fairly well in the low-wavenumber region and deviate in the high-wavenumber region. This is consistent with expectations, since the dynamics of the larger-scale motions (corresponding to smaller κ_x) are computed explicitly in LES and the influence of the smaller scales (corresponding to larger κ_x) is taken care of by the turbulent model. Hence, the LES is not able to compute the spectral density accurately at high wavenumbers (small motion scales). Moreover, the mesh in LES is coarser than that in DNS, and the maximum resolved wavenumber is thus lower in LES. As a result, the LES results show a drop of the spectral density at large wavenumbers compared to the DNS results, for all three velocity components. Evidently, current LES can capture the Kolmogorov $-5/3$ spectrum in the inertial subrange for all velocity components, which also shows good universality among different Reynolds numbers and y locations. Further inspection of the velocity spectra shows that the LES results
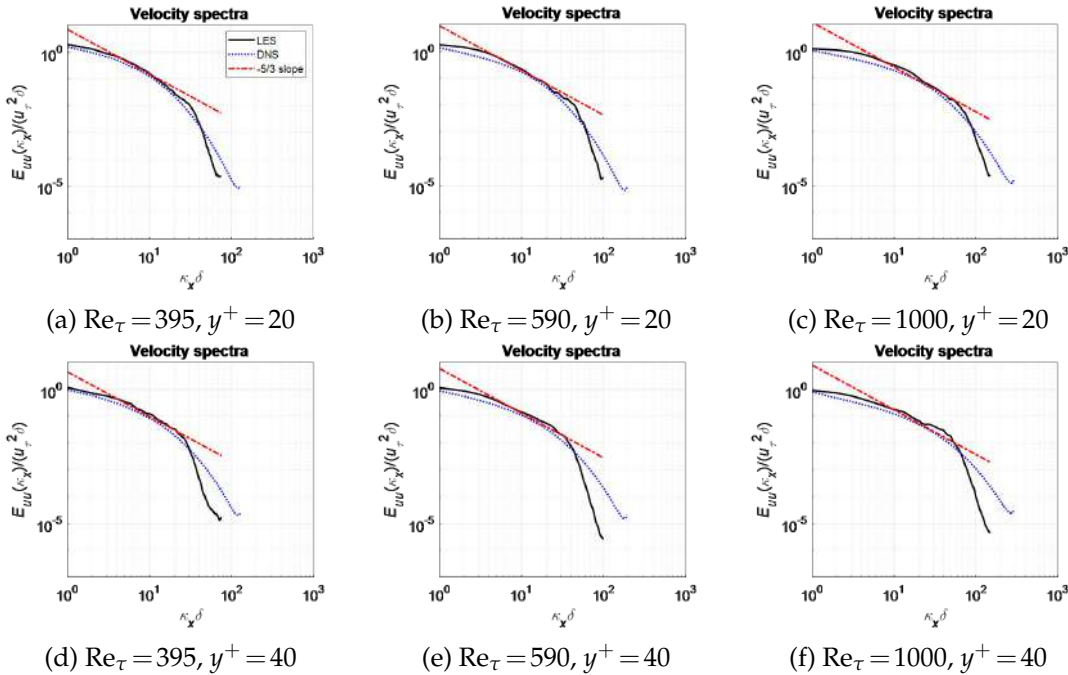

Figure 7: Streamwise $(x-)$ one-dimensional velocity spectrum $(E_{uu}(\kappa_x))$ at indicated y locations. The DNS results at $Re_\tau = 395$ and 590 are from Moser et al. [36] and those at $Re_\tau = 1000$ are from Lee and Moser [37], so are the results presented in Fig. 8 and Fig. 9.
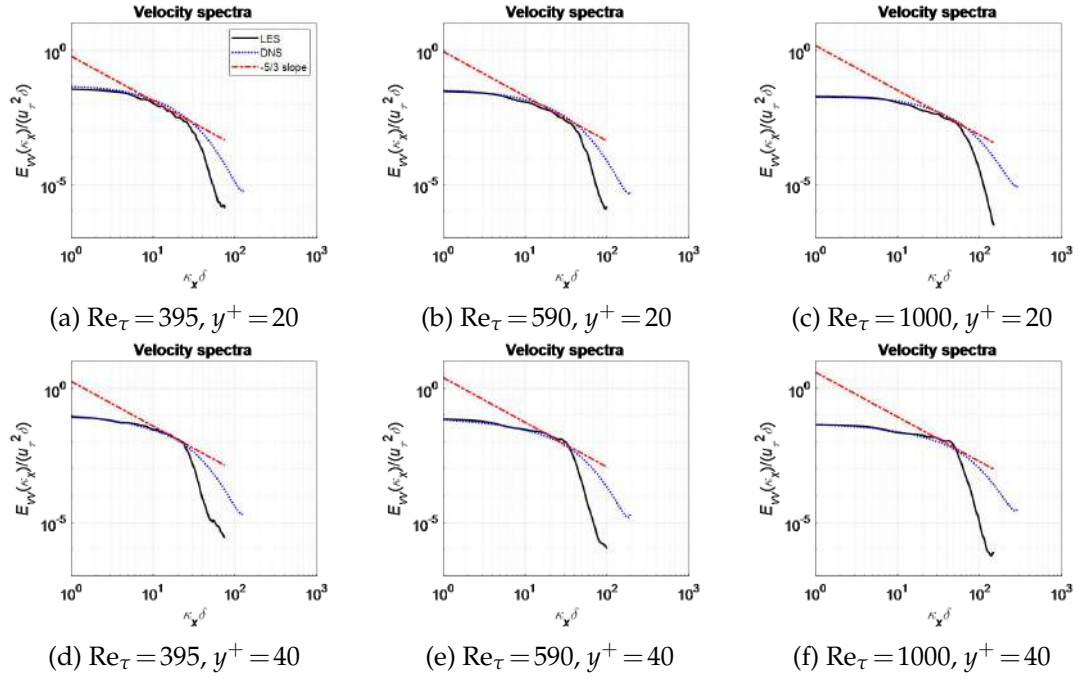
(a) $\text{Re}_\tau = 395$, $y^+ = 20$

(b) $\text{Re}_\tau = 590$, $y^+ = 20$

(c) $\text{Re}_\tau = 1000$, $y^+ = 20$

(d) $\text{Re}_\tau = 395$, $y^+ = 40$

(e) $\text{Re}_\tau = 590$, $y^+ = 40$

(f) $\text{Re}_\tau = 1000$, $y^+ = 40$

Figure 8: Streamwise $(x-)$ one-dimensional velocity spectrum $(E_{vv}(\kappa_x))$ at indicated y locations.

can match the DNS results up to a higher wavenumber at smaller y location ($y^+ = 20$ versus 40). This means that the region nearer to the wall is better resolved, which is intended in current wall-resolved LES and agrees well with the turbulent statistics in the preceding sections. Notably, the spectral density decreases rapidly as the wavenumber increases, which shows that the bulk of the turbulent kinetic energy is contained in the low-wavenumber (large-scale) motions. This is also consistent to the analysis of the turbulent kinetic energy in Section 4.4. Last but not least, the good match of the LES results and the DNS results at different Reynolds numbers verifies that the mesh configuration determined by the grid size scaling law can capture the velocity spectra reasonably well as the Reynolds number varies.

4.6 Flow structures

Streaks are very important flow structures and show up frequently in wall-bounded turbulent shear flows, which represent elongated regions with low instantaneous streamwise velocity. On the other hand, the fluid between the streaks moves relatively faster. Streaks have been visualized in the near-wall region in both experiments and numerical simulations [40, 45–47]. Near the wall, the streaks are randomly distributed with a spacing of approximately 80 to 120 wall units (δv), which is independent of the Reynolds
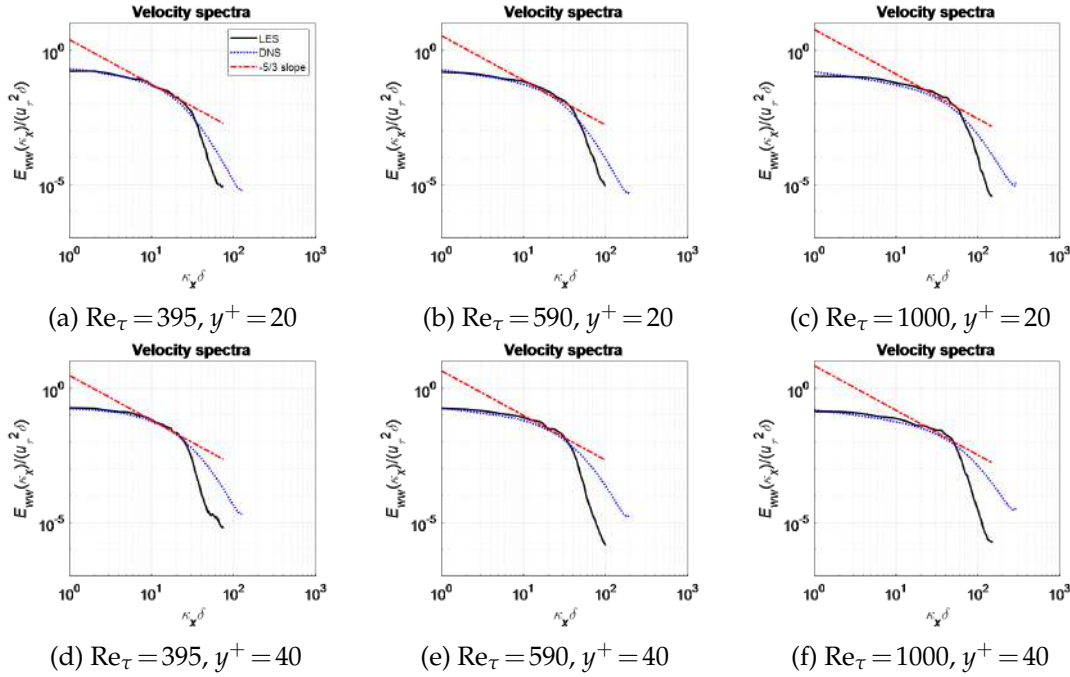
Figure 9: Streamwise ($x-$) one-dimensional velocity spectrum ($E_{ww}(\kappa_x)$) at indicated y locations.

number [25]. The streak patterns are visualized in Figs. 10(a)-(c), where the instantaneous velocity contours are plotted in the wall-parallel planes at $y^+ = 15$. It can be found that the distribution of streaks agrees well with that reported in literature, which exhibits a spacing of around 100 wall units (δv) and shows no dependency on the Reynolds number. In the near-wall region, streamwise vortices (rolls) are identified as the dominant vortical structures for a turbulent flow [48,49]. Such streamwise vortices lift up the slow-moving fluid near the wall on one side (left or right side of the vortex core), while bringing down the fast-moving fluid away from the wall on the other side, which contributes to the streaks in the wall-parallel planes. Head and Bandyopadhyay [50] suggested that the streamwise vortices further stretch away from the wall to form horseshoe (hairpin) vortices. The near-wall vortical structures are visualized by λ_2 iso-surfaces at $Re_\tau = 395$ in Fig. 10(d). The streamwise vortices near the wall can be identified clearly, including the upward stretching at the downstream and the appearance of horseshoe vortices (indicated by the dashed curves). We can thus conclude that the current LES is capable of capturing the important turbulent flow structures reasonably well. Moreover, consistent flow topology can be obtained as the mesh size scaling law is satisfied.
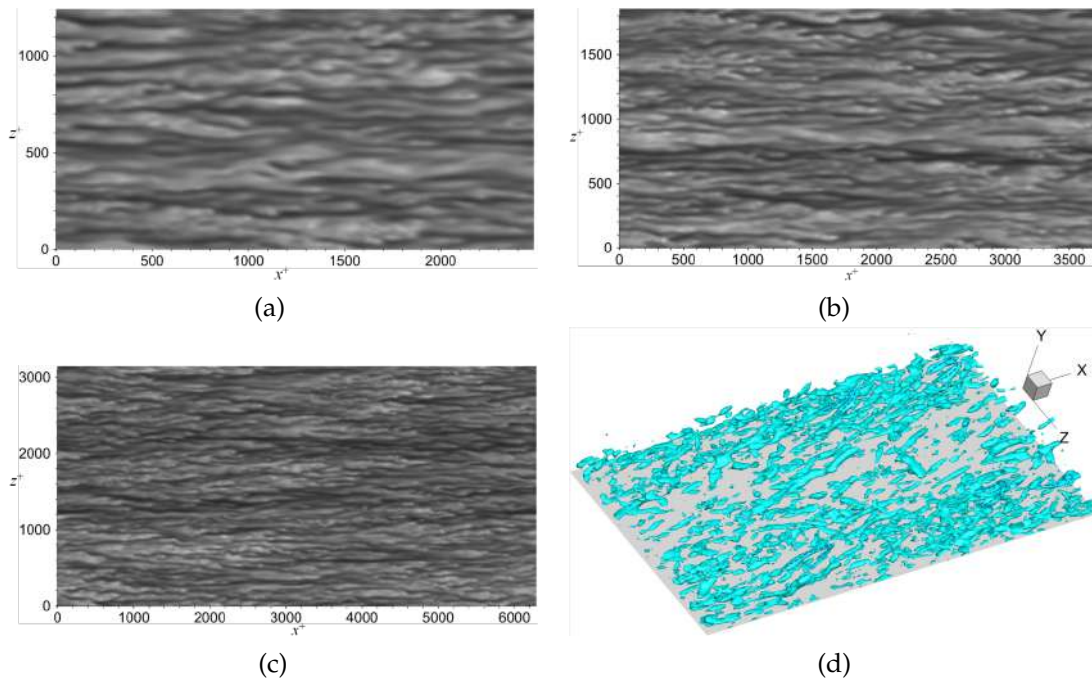
Figure 10: Near-wall streaks and vortical structures. (a), (b) and (c) show the streak patterns at $y^+ = 15$ for $Re_\tau = 395$, 590 and 1000, respectively. Dark regions represent low speed regions, whereas bright regions represent high speed regions. (d) shows the near-wall vortical structures at $Re_\tau = 395$, vortex strands are visualized by iso-surfaces of $\lambda_2 = -0.0025$, normalized by inner units.

5 Conclusions

In this paper, large eddy simulation (LES) is applied to a turbulent plane channel flow, where a grid size scaling law is developed to determine the appropriate mesh configuration as the Reynolds number is varied. An optimal mesh configuration is firstly determined at a relatively low Reynolds number ($Re_\tau = 395$), which shows good balance between computational accuracy and cost. The mesh configurations at higher Reynolds numbers can thus be determined with the mesh size scaling law. Simulations have been conducted at various Reynolds numbers ($Re_\tau = 395$, 590 and 1000) to validate the grid size scaling law with extensive comparison against published results. The current LES is able to predict the mean velocity profile accurately for all Reynolds numbers under investigation. The von Káarmán constant obtained in the current study agrees well with that reported in the literature. Good linear variation of the total shear stress with distance from the channel wall is obtained in the current study, which is an important distinguishing feature for a plane channel flow. In addition, the grid-scale Reynolds stress tensor is calculated with reasonably good accuracy. By taking both the grid-scale and subgrid-scale turbulent kinetic energy (TKE) into consideration, the overall TKE matches

surprisingly well with that from DNS studies in the near-wall region. Good balance of the TKE budget is also obtained by formulating the grid-scale TKE transport equation in LES. The velocity spectra obtained from LES are consistent with that from DNS, especially in the low-wavenumber region. Meanwhile, the Kolmogorov $-5/3$ power law is evident in the spectra. This suggests that the bulk of the turbulent kinetic energy can be resolved directly, which is intended in current LES. Lastly, the near-wall streaks and vortical structures can be well captured. Hence, we can conclude that reasonably accurate results can be obtained with the current LES. More importantly, extensive validation has shown that the variation of the results with Reynolds number is consistent with that for DNS if the grid size scaling law is satisfied. We can thus obtain reasonably good predictions for flows at even higher Reynolds numbers with significantly lower computational costs compared to DNS. Last but not the least, the current LES may also be applied to other wall bounded turbulent shear flows, such as pipe flows, boundary layer flows and channel flows with modified geometries and boundary conditions. The reason is because sufficiently good near-wall resolution is used in the current wall-resolved LES, and the near-wall viscous region is resolved in nearly the same manner as DNS. In addition, the selection of the power coefficient in the grid size scaling law corresponds to the value in the range of $40 < y^+ < 150$ (see the discussion in Section 3), where the variation of physical quantities is relatively less dependent on the boundary. On the other hand, validation and grid size testing are still essential at low Reynolds numbers to find out the appropriate mesh configuration, before the mesh size scaling law can be applied. Similar mesh size scaling law and LES model have been applied in the study of turbulent flow drag reduction by the superhydrophobic surface [51], which has more complex boundary conditions than plane channel flows.

Appendix A: Numerical schemes in OpenFOAM

In this section, the original NS equation for incompressible flows (without turbulence modelling) is considered to illustrate the numerical schemes in OpenFOAM. Simple schemes are selected for the purpose of demonstration, which might be different from the schemes used in the present study.

Discretization

Integrating the NS equation

$$\left(\frac{\partial \mathbf{U}}{\partial t} + \nabla \cdot (\mathbf{U}\mathbf{U}) - \nabla \cdot (\nu \nabla \mathbf{U}) + \nabla p = 0\right)$$

over the cell volume V centered at the point P yields and applying the Gauss theorem (S stands for cell face area) result in the following:

$$\frac{\partial \mathbf{U}_P}{\partial t} + \frac{1}{V}\sum_f \mathbf{U}_f \phi_f - \frac{1}{V}\sum_f \nu \left(\mathbf{n}_f \cdot \nabla \mathbf{U}_f\right) S_f + \frac{1}{V}\sum_f p_f \mathbf{n}_f S_f = 0,$$

where $\phi = \mathbf{U} \cdot \mathbf{n} S_f$ is defined as the surface flux, $\mathbf{U}_f$ and p_f are the cell face values.

The terms in the above equations are discretized or interpolated as follows (Euler backward scheme used for simplicity)

$$\left(\frac{1}{\Delta t} + \sum_f \left(\phi_f a_{fP} - \nu a'_{fP}\right)\right)\mathbf{U}_P^{n+1} + \sum_f \left(\phi_f a_{fN} - \nu a'_{fN}\right)\mathbf{U}_{fN}^{n+1}$$

$$+ \sum_f \left(a''_{fP} p_P^{n+1} + a''_{fN} p_{fN}^{n+1}\right)\mathbf{n}_f = \frac{1}{\Delta t}\mathbf{U}_P^n.$$

The letters (a, a', a'') represent the discretization/interpolation coefficients containing the mesh geometry information and boundary conditions, the values of which depend on the schemes. N stands for the neighboring cell centre. The reader may refer to the Open-FOAM documentation for more details about different discretization schemes.

Defining vectors

$$\mathbf{x}_1 = \begin{pmatrix} U_1 \\ U_2 \\ \vdots \\ U_{M-1} \\ U_M \end{pmatrix}, \quad \mathbf{x}_2 = \begin{pmatrix} V_1 \\ V_2 \\ \vdots \\ V_{M-1} \\ V_M \end{pmatrix}, \quad \mathbf{x}_3 = \begin{pmatrix} W_1 \\ W_2 \\ \vdots \\ W_{M-1} \\ W_M \end{pmatrix}, \quad \mathbf{x}_4 = \begin{pmatrix} p_1 \\ p_2 \\ \vdots \\ p_{M-1} \\ p_M \end{pmatrix},$$

where M is the total number of computational cells. The above discretization of the x-momentum equation for all computational cells can be written as follows:

$$\left(\frac{1}{\Delta t}\mathbf{I} + \mathbf{B}\right)\mathbf{x}_1^{n+1} = \frac{1}{\Delta t}\mathbf{x}_1^n - \mathbf{C}_x \mathbf{x}_4^{n+1}.$$

Similarly, the y-momentum equation and the z-momentum equation can be derived for $\mathbf{x}_2$ and $\mathbf{x}_3$.

Pressure Poisson equation

Velocity ($\mathbf{x}_1$, $\mathbf{x}_2$ and $\mathbf{x}_3$) and pressure ($\mathbf{x}_4$) are coupled in the above linear system of equations, which is usually not solved directly. In the PISO algorithm, the linear system of equations is split into an implicit predictor step and multiple explicit corrector steps. A pressure Poisson equation is formed for the corrector step in the PISO algorithm

$$\left(\frac{1}{\Delta t} + \sum_f \left(\phi_f a_{fP} - \nu a'_{fP}\right)\right)\mathbf{U}_P^{n+1} + \sum_f \left(\phi_f a_{fN} - \nu a'_{fN}\right)\mathbf{U}_{fN}^{n+1} = \frac{1}{\Delta t}\mathbf{U}_P^n - \nabla p_P^{n+1}$$

is exact and can be rearranged as follows:

$$\mathbf{U}_P^{n+1} = \frac{1}{\left(\frac{1}{\Delta t} + \sum_f \left(\phi_f a_{fP} - \nu a'_{fP}\right)\right)} \left(\frac{1}{\Delta t}\mathbf{U}_P^n - \sum_f \left(\phi_f a_{fN} - \nu a'_{fN}\right)\mathbf{U}_{fN}^{n+1} - \nabla p_P^{n+1}\right),$$

$$\mathbf{U}_P^{n+1} = \frac{1}{A_P}\left(\frac{1}{\Delta t}\mathbf{U}_P^n - \sum_f A_{PN}\mathbf{U}_{fN}^{n+1} - \nabla p_P^{n+1}\right),$$

with

$$A_P = \frac{1}{\Delta t} + \sum_f \left(\phi_f a_{fP} - \nu a'_{fP}\right)$$

are the diagonal entries of the matrix

$$\left(\frac{1}{\Delta t}\mathbf{I} + \mathbf{B}\right) \quad \text{and} \quad A_{PN} = \phi_f a_{fN} - \nu a'_{fN}$$

are the off-diagonal entries.

Defining vector

$$\mathbf{h}_P^{n+1} = \frac{1}{\Delta t}\mathbf{U}_P^n - \sum_f A_{PN}\mathbf{U}_{fN}^{n+1} \quad \text{(source term minus off-diagonal terms)},$$

we can further define another vector

$$\mathbf{u}_{P,HbyA}^{n+1} = \frac{\mathbf{h}_P^{n+1}}{A_P} = \frac{\mathbf{U}_P^n}{\Delta t A_P} - \frac{\sum_f A_{PN}\mathbf{U}_{fN}^{n+1}}{A_P}$$

and construct a $3 \times M$ matrix

$$\mathbf{K}_{HbyA}^{n+1} = \left[\mathbf{u}_{P,HbyA}^{n+1}\right]_{P=1,2,3,\cdots,M}.$$

Hence, we have

$$\mathbf{U}_P^{n+1} = \mathbf{u}_{P,HbyA}^{n+1} - \frac{1}{A_P}\nabla p_P^{n+1}.$$

The values of $\mathbf{U}^{n+1}$, $\mathbf{u}_{HbyA}^{n+1}$ and ∇p^{n+1} are interpolated from cell centres to cell faces and

$$\mathbf{U}_{P,f}^{n+1} = \mathbf{u}_{P,f,HbyA}^{n+1} - \frac{1}{A_{P,f}}\nabla p_{P,f}^{n+1}$$

is derived.

According to the continuity equation,

$$\nabla \cdot \mathbf{U}_P^{n+1} = 0,$$

we thus have:

$$\sum_f \mathbf{U}_{P,f}^{n+1} \cdot \mathbf{n}_f S_f = \sum_f \left(\mathbf{u}_{P,f,HbyA}^{n+1} - \frac{1}{A_{P,f}} \nabla p_{P,f}^{n+1} \right) \cdot \mathbf{n}_f S_f = 0,$$

$$\sum_f \frac{1}{A_{P,f}} \nabla p_{P,f}^{n+1} \cdot \mathbf{n}_f S_f = \sum_f \mathbf{u}_{P,f,HbyA}^{n+1} \cdot \mathbf{n}_f S_f.$$

If we ignore the difference between A_P and $A_{P,f}$, the above equation is the discretized form of

$$\frac{1}{A_P} \int_V \nabla^2 p_P^{n+1} dV = \int_V \nabla \cdot \mathbf{u}_{P,HbyA}^{n+1} dV.$$

Hence, the pressure Poisson equation is derived as follows:

$$\frac{1}{A_P} \nabla^2 p_P^{n+1} = \nabla \cdot \mathbf{u}_{P,HbyA}^{n+1}.$$

p_P^{n+1} can be solved from the above pressure Poisson equation. Hence,

$$\frac{1}{A_P} \int_S \mathbf{n}_f \cdot \nabla p_f^{n+1} dS = \int_S \mathbf{n}_f \cdot \mathbf{u}_{P,f,HbyA}^{n+1} dS,$$

$$\frac{1}{A_P} \sum_f S_f \left(g_{fP} p_P^{n+1} + g_{fN} p_{fN}^{n+1} \right) = \sum_f \mathbf{n}_f \cdot \mathbf{u}_{P,f,HbyA}^{n+1} S_f,$$

$$\frac{1}{A_P} \left(\sum_f S_f g_{fP} \right) p_P^{n+1} + \frac{1}{A_P} \sum_f S_f g_{fN} p_{fN}^{n+1} = \sum_f \phi_{P,f,HbyA}^{n+1}.$$

The above discretization (the letter g represents discretization coefficients) for all computational cells can be written as follows

$$\mathbf{G} \mathbf{x}_4^{n+1} = \left[\sum_f \phi_{f,HbyA} \right]^{n+1}.$$

PISO algorithm

Predictor

$$A_P \mathbf{U}_P^r + \sum_f A_{PN} \mathbf{U}_{fN}^r = \frac{1}{\Delta t} \mathbf{U}_P^n - \nabla p_P^n$$

is solved with the Gauss-Seidel smooth solver. In the form of a linear matrix system $(\mathbf{Ax}=\mathbf{b})$,

$$
\begin{cases}
\left(\dfrac{1}{\Delta t}\mathbf{I}+\mathbf{B}\right)\mathbf{x}_1^r = \dfrac{1}{\Delta t}\mathbf{x}_1^n - \mathbf{C}_x\mathbf{x}_4^n, \\[2mm]
\left(\dfrac{1}{\Delta t}\mathbf{I}+\mathbf{B}\right)\mathbf{x}_2^r = \dfrac{1}{\Delta t}\mathbf{x}_2^n - \mathbf{C}_y\mathbf{x}_4^n, \\[2mm]
\left(\dfrac{1}{\Delta t}\mathbf{I}+\mathbf{B}\right)\mathbf{x}_3^r = \dfrac{1}{\Delta t}\mathbf{x}_3^n - \mathbf{C}_z\mathbf{x}_4^n.
\end{cases}
$$

Corrector

The intermediate velocity and pressure are denoted by $\mathbf{U}^*$ and p^*, respectively.

Let $\mathbf{U}^*=\mathbf{U}^r$. The following quantities are derived:

$$
\mathbf{u}_{P,HbyA}^* = \frac{\mathbf{U}_P^n}{\Delta t A_P} - \frac{\sum\limits_f A_{PN}\mathbf{U}_{fN}^*}{A_P}
\quad\text{and}\quad
\phi_{P,f,HbyA}^* = \mathbf{u}_{P,f,HbyA}^* \cdot \mathbf{n}_f S_f.
$$

The pressure Poisson equation is solved for p^* with the GAMG solver:

$$
\frac{1}{A_P}\left(\sum_f S_f g_{fP}\right)p_P^* + \frac{1}{A_P}\sum_f S_f g_{fN} p_{fN}^* = \sum_f \phi_{P,f,HbyA}^*.
$$

In the form of a linear matrix system $(\mathbf{Ax}=\mathbf{b})$,

$$
\mathbf{G}\mathbf{x}_4^* = \left[\sum_f \phi_{f,HbyA}\right]^*.
$$

$\mathbf{U}^*$ is updated using

$$
\mathbf{U}_P^* = \mathbf{u}_{P,HbyA}^* - \frac{1}{A_P}\nabla p_P^*.
$$

The above two steps are repeated until convergence is achieved, then

$$
\mathbf{U}^{n+1}=\mathbf{U}^*, \quad p^{n+1}=p^*.
$$

The PISO algorithm can be summarized with the figure below.

Appendix B: Grid-scale TKE transport equation in LES

Mean momentum equation:

$$
\frac{\partial\langle\bar{U}_j\rangle}{\partial t} + \frac{\partial\langle\bar{U}_i\rangle\langle\bar{U}_j\rangle}{\partial x_i} = v\frac{\partial^2\langle\bar{U}_j\rangle}{\partial x_i\partial x_i} - \frac{1}{\rho}\frac{\partial\langle\tilde{p}\rangle}{\partial x_j} - \frac{\partial\langle\bar{u}_i\bar{u}_j\rangle}{\partial x_i} - \frac{\partial\left\langle\tau_{ij}^D\right\rangle}{\partial x_i},
$$

$$
\frac{\partial\langle\bar{U}_j\rangle}{\partial t} + \frac{\partial\langle\bar{U}_i\rangle\langle\bar{U}_j\rangle}{\partial x_i} = v\frac{\partial^2\langle\bar{U}_j\rangle}{\partial x_i\partial x_i} - \frac{1}{\rho}\frac{\partial\langle\tilde{p}\rangle}{\partial x_j} - \frac{\partial\langle\bar{u}_i\bar{u}_j\rangle}{\partial x_i} + \frac{\partial\langle 2v_t\bar{S}_{ij}\rangle}{\partial x_i}.
$$

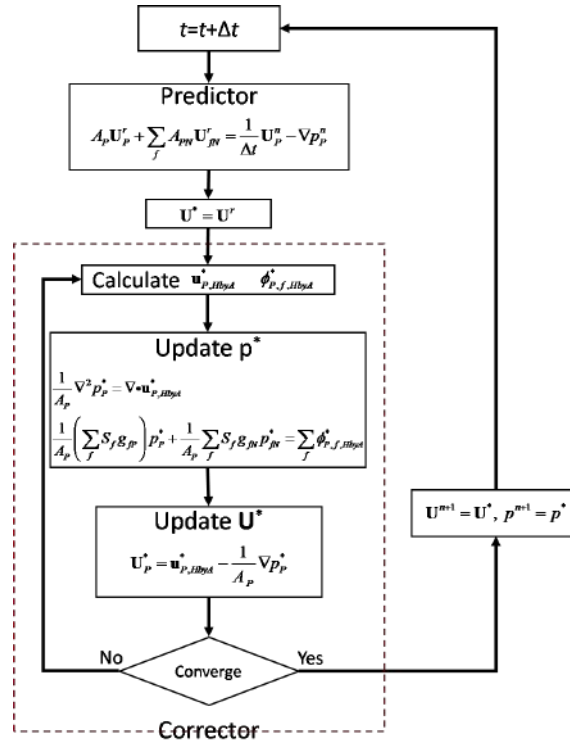Figure 11: Flow chart for the PISO algorithm.

Fluctuating momentum equation:

$$
\frac{\partial \bar{u}_j}{\partial t} + \frac{\partial \bar{u}_i \langle \bar{U}_j \rangle}{\partial x_i} + \frac{\partial \langle \bar{U}_i \rangle \bar{u}_j}{\partial x_i} + \frac{\partial \bar{u}_i \bar{u}_j}{\partial x_i}
$$
$$
= v \frac{\partial^2 \bar{u}_j}{\partial x_i \partial x_i} - \frac{1}{\rho} \frac{\partial \tilde{p}'}{\partial x_j} + \frac{\partial \langle \bar{u}_i \bar{u}_j \rangle}{\partial x_i} + \frac{\partial \tau_{ij}^D}{\partial x_i} - \frac{\partial \langle \tau_{ij}^D \rangle}{\partial x_i}.
$$

Multiplying the fluctuating momentum equation by $\bar{u}_j$

$$
\bar{u}_j \frac{\partial \bar{u}_j}{\partial t} + \bar{u}_j \frac{\partial \bar{u}_i \langle \bar{U}_j \rangle}{\partial x_i} + \bar{u}_j \frac{\partial \langle \bar{U}_i \rangle \bar{u}_j}{\partial x_i} + \bar{u}_j \frac{\partial \bar{u}_i \bar{u}_j}{\partial x_i}
$$
$$
= v \bar{u}_j \frac{\partial^2 \bar{u}_j}{\partial x_i \partial x_i} - \frac{1}{\rho} \bar{u}_j \frac{\partial \tilde{p}'}{\partial x_j} + \bar{u}_j \frac{\partial \langle \bar{u}_i \bar{u}_j \rangle}{\partial x_i} + \bar{u}_j \frac{\partial \tau_{ij}^D}{\partial x_i} - \bar{u}_j \frac{\partial \langle \tau_{ij}^D \rangle}{\partial x_i}.
$$

Take the mean of the above equation to derive the grid-scale turbulent kinetic energy $(k_{gs} = \langle \bar{u}_i \bar{u}_i \rangle / 2)$ equation:

$$\frac{\partial k_{gs}}{\partial t} + \langle \bar{U}_i \rangle \frac{\partial k_{gs}}{\partial x_i}$$

$$= \underbrace{-\langle \bar{u}_i \bar{u}_j \rangle \frac{\partial \langle \bar{U}_j \rangle}{\partial x_i}}_{\text{production } (\mathcal{P})} \underbrace{-\frac{1}{2} \frac{\partial \langle \bar{u}_i \bar{u}_j \bar{u}_j \rangle}{\partial x_i}}_{\text{turbulent transport}} \underbrace{+\nu \frac{\partial^2 k_{gs}}{\partial x_i \partial x_i}}_{\text{viscous diffusion}} \underbrace{-\nu \left\langle \frac{\partial \bar{u}_j}{\partial x_i} \frac{\partial \bar{u}_j}{\partial x_i} \right\rangle}_{\text{dissipation } (\varepsilon)} \underbrace{-\frac{1}{\rho} \frac{\partial \langle \bar{u}_i \tilde{p}' \rangle}{\partial x_i}}_{\text{pressure transport}}$$

$$-\left\langle \bar{u}_j \frac{\partial \tau_{ij}^D}{\partial x_i} \right\rangle.$$

References

[1] J. SMAGORINSKY, *General circulation experiments with the primitive equations: I. The basic experiment,* Monthly Weather Rev., 1963. 91(3) (1963), pp. 99–164.

[2] M. GERMANO ET AL., *A dynamic subgrid-scale eddy viscosity model,* Phys. Fluids A Fluid Dyn., 3(7) (1991), pp. 1760–1765.

[3] D. K. LILLY, *A proposed modification of the Germano subgrid-scale closure method,* Phys. Fluids A Fluid Dyn., 4(3) (1992), pp. 633–635.

[4] C. MENEVEAU, T. S. LUND, AND W. H. CABOT, *A Lagrangian dynamic subgrid-scale model of turbulence,* J. Fluid Mech., 319 (1996), pp. 353–385.

[5] Y. ZANG, R. L. STREET, AND J. R. KOSEFF, *A dynamic mixed subgrid-scale model and its application to turbulent recirculating flows,* Phys. Fluids A Fluid Dyn., 5(12) (1993), pp. 3186–3196.

[6] B. VREMAN, B. GEURTS, AND H. KUERTEN, *On the formulation of the dynamic mixed subgrid-scale model,* Phys. Fluids, 6(12) (1994), pp. 4057–4059.

[7] O. MÉTAIS, AND M. LESIEUR, *Spectral large-eddy simulation of isotropic and stably stratified turbulence,* J. Fluid Mech., 239 (1992), pp. 157–194.

[8] M. LESIEUR, AND O. METAIS, *New trends in large-eddy simulations of turbulence,* Ann. Rev. Fluid Mech., 28(1) (1996), pp. 45–82.

[9] F. NICOUD, AND F. DUCROS, *Subgrid-scale stress modelling based on the square of the velocity gradient tensor,* Flow Turbul. Combus., 62(3) (1999), pp. 183–200.

[10] W. ROZEMA ET AL., *Minimum-dissipation models for large-eddy simulation,* Phys. Fluids, 27(8) (2015), 085107.

[11] A. P. ZAHIRI, AND E. ROOHI, *Anisotropic minimum-dissipation (AMD) subgrid-scale model implemented in OpenFOAM: verification and assessment in single-phase and multi-phase flows,* Comput. Fluids, 180 (2019), pp. 190–205.

[12] A. P. ZAHIRI, AND E. ROOHI, *Assessment of anisotropic minimum-dissipation (AMD) subgrid-scale model: Gently-curved backward-facing step flow,* Int. J. Modern Phys. C, 32(05) (2021), 2150068.

[13] J. DEARDORFF, *The use of subgrid transport equations in a three-dimensional model of atmospheric turbulence,* J. Fluids Eng., 95(3) (1973), pp. 429–438.

[14] U. SCHUMANN, *Subgrid scale model for finite difference simulations of turbulent flows in plane channels and annuli,* J. Comput. Phys., 18(4) (1975), pp. 376–404.

[15] A. YOSHIZAWA, AND K. HORIUTI, *A statistically-derived subgrid-scale kinetic energy model for the large-eddy simulation of turbulent flows,* Journal of the Physical Society of Japan, 54(8) (1985), pp. 2834–2839.

[16] S. GHOSAL ET AL., *A dynamic localization model for large-eddy simulation of turbulent flows,* J. Fluid Mech., 286 (1995), pp. 229–255.

[17] C. FUREBY, ET AL., *Differential subgrid stress models in large eddy simulations,* Phys. Fluids, 9(11) (1997), pp. 3578–3580.

[18] S. KRAJNOVIĆ, AND L. DAVIDSON, *A mixed one-equation subgrid model for large-eddy simulation,* Int. J. Heat Fluid Flow, 23(4) (2002), pp. 413–425.

[19] F. GALLERANO, E. PASERO, AND G. CANNATA, *A dynamic two-equation sub grid scale model,* Continuum Mech. Thermodyn., 17(2) (2005), pp. 101–123.

[20] J. P. BORIS, On Large Eddy Simulation Using Subgrid Turbulence Models Comment 1, in Whither Turbulence? Turbulence at the Crossroads, 1990, Springer, pp. 344–353.

[21] T. TAMURA, AND K. KUWAHARA, *Numerical analysis on aerodynamic characteristics of an inclined square cylinder,* 20th Fluid Dynamics, Plasma Dynamics and Lasers Conference, 1989.

[22] D. KNIGHT, ET AL., *Compressible large eddy simulation using unstructured grids,* 36th AIAA Aerospace Sciences Meeting and Exhibit, 1998.

[23] G. URBIN, AND D. KNIGHT, *Large-eddy simulation of a supersonic boundary layer using an unstructured grid,* AIAA J., 39(7) (2001), pp. 1288–1295.

[24] C. MENEVEAU, AND J. KATZ, *Scale-invariance and turbulence models for large-eddy simulation,* Ann. Rev. Fluid Mech., 32(1) (2000), pp. 1–32.

[25] S. B. POPE, Turbulent Flows, Cambridge University Press, (2000).

[26] Y. ZHIYIN, *Large-eddy simulation: Past, present and the future,* Chinese J. Aeron., 28(1) (2015), pp. 11–24.

[27] U. PIOMELLI, AND E. BALARAS, *Wall-layer models for large-eddy simulations,* Ann. Rev. Fluid Mech., 34(1) (2002), pp. 349–374.

[28] U. PIOMELLI, *Wall-layer models for large-eddy simulations,* Prog. Aerospace Sci., 44(6) (2008), pp. 437–446.

[29] S. REZAEIRAVESH, AND M. LIEFVENDAHL, *Effect of grid resolution on large eddy simulation of wall-bounded turbulence,* Phys. Fluids, 30(5) (2018), 055106.

[30] K. LILLY, The Representation of Small-Scale Turbulence in Numerical Simulation Experiments, 1966.

[31] J. W. DEARDORFF, *A numerical study of three-dimensional turbulent channel flow at large Reynolds numbers,* J. Fluid Mech., 41(2) (1970), pp. 453–480.

[32] P. MOIN, AND J. KIM, *Numerical investigation of turbulent channel flow,* J. Fluid Mech., 118 (1982), pp. 341–377.

[33] E. R. VAN DRIEST, *On turbulent flow near a wall,* J. Aeronautical Sci., 23(11) (1956), pp. 1007–1011.

[34] U. PIOMELLI, *High Reynolds number calculations using the dynamic subgrid-scale stress model,* Phys. Fluids A Fluid Dyn., 5(6) (1993), pp. 1484–1490.

[35] E. LENORMAND, ET AL., *Subgrid-scale models for large-eddy simulations of compressible wall bounded flows,* AIAA J., 38(8) (2000), pp. 1340–1350.

[36] R. D. MOSER, J. KIM, AND N. N. MANSOUR, *Direct numerical simulation of turbulent channel flow up to $Re_\tau = 590$,* Phys. Fluids, 11(4) (1999), pp. 943–945.

[37] M. LEE, AND R. D. MOSER, *Direct numerical simulation of turbulent channel flow up to $Re_\tau = 5200$,* J. Fluid Mech., 774 (2015), pp. 395–415.

[38] D. R. CHAPMAN, *Computational aerodynamics development and outlook,* AIAA J., 17(12) (1979),

pp. 1293–1313.

[39] A. LOZANO-DURÁN, AND J. JIMÉNEZ, *Effect of the computational domain on direct simulations of turbulent channels up to $Re_\tau = 4200$*, Phys. Fluids, 26(1) (2014), 011702.

[40] M. BERNARDINI, S. PIROZZOLI, AND P. ORLANDI, *Velocity statistics in turbulent channel flow up to $Re_\tau = 4000$*, J. Fluid Mech., 742 (2014), pp. 171–191.

[41] M. P. SCHULTZ, AND K. A. FLACK, *Reynolds-number scaling of turbulent channel flow,* Phys. Fluids, 25(2) (2013), 025104.

[42] D. CHATZIKYRIAKOU, ET AL., *DNS and LES of turbulent flow in a closed channel featuring a pattern of hemispherical roughness elements,* Int. J. Heat Fluid Flow, 53 (2015), pp. 29–43.

[43] E. LAR KERMANI, E. ROOHI, AND F. PORTÉE-AGEL, *Evaluating the modulated gradient model in large eddy simulation of channel flow with OpenFOAM,* J. Turbul., 19(7) (2018), pp. 600–620.

[44] L. A. SCHIAVO, W. R. WOLF, AND J. L. F. AZEVEDO, *Turbulent kinetic energy budgets in wall bounded flows with pressure gradients and separation,* Phys. Fluids, 29(11) (2017), 115108.

[45] S. J. KLINE, ET AL., *The structure of turbulent boundary layers,* J. Fluid Mech., 30(4) (1967), pp. 741–773.

[46] H. S. KIM, S. KLINE, AND W. REYNOLDS, *The production of turbulence near a smooth wall in a turbulent boundary layer,* Journal of Fluid Mech., 50(1) (1971), pp. 133–160.

[47] C. SMITH, AND S. METZLER, *The characteristics of low-speed streaks in the near-wall region of a turbulent boundary layer,* J. Fluid Mech., 129 (1983), pp. 27–54.

[48] H. P. BAKEWELL JR, AND J. L. LUMLEY, *Viscous sublayer and adjacent wall region in turbulent pipe flow,* The Phys. Fluids, 10(9) (1967), pp. 1880–1889.

[49] R. BLACKWELDER, AND J. HARITONIDIS, *Scaling of the bursting frequency in turbulent boundary layers,* J. Fluid Mech., 132 (1983), pp. 87–103.

[50] M. HEAD, AND P. BANDYOPADHYAY, *New aspects of turbulent boundary-layer structure,* J. Fluid Mech., 107 (1981), pp. 297–338.

[51] J. YAO, AND C. TEO, *Effect of the liquid–gas interface curvature for a superhydrophobic surface with longitudinal grooves in turbulent flows,* Phys. Fluids, 33(7) (2021), 075116.